STATE OF OREGON
DEPARTMENT OF GEOLOGY AND MINERAL INDUSTRIES
RUARRI J. DAY-STIRRAT, STATE GEOLOGIST
https://www.oregon.gov/dogami

Text to Accompany the Geologic Map of the Adams 7.5′ Quadrangle, Umatilla County, Oregon

2026

GMS-134

Geologic Map of the Adams 7.5′ Quadrangle, Umatilla County, Oregon

by Carlie J.M. Azzopardi[1], Jason D. McClaughry[1,2], David R. Gaylord[3],
Eduardo F. Guerrero[1], and Lowell H. Anthony[1]

Cartography by Jon J. Franczyk[1] and Geodatabase by Carlie J.M. Azzopardi[1]

[1]Oregon Department of Geology and Mineral Industries, 800 NE Oregon Street, Suite 965, Portland, OR 97232
[2]Oregon Department of Geology and Mineral Industries, Baker City Field Office, Baker County Courthouse, 1995 3rd Street, Suite 130, Baker City, OR 97814
[3]School of the Environment, College of Arts and Sciences, Washington State University, Pullman, WA 99164

PLATE 2

INTRODUCTION

The Adams 7.5′ quadrangle in Umatilla County of northeast Oregon includes an area of 134 square kilometers (km^2) at the eastern edge of the Columbia Plateau, a broad depression forming the northwestern flank of the Blue Mountains (Figure 1). The oldest rocks in the map area are part of the ~17- to 6-million-year-old Columbia River Basalt Group (CRBG), a succession of tholeiitic basalt and basaltic andesite lava flows cropping out over more than 210,000 km^2 in parts of Washington, Oregon, Idaho, and Nevada (Reidel and others, 2013a; Figures 1, 2; Plate 1). The CRBG is largely overlain by Pleistocene to Holocene loess across the map area and Pleistocene and Holocene alluvial units on valley floors (Plate 1). Three major fault zones converge in this part of the Columbia Plateau, including the WNW-striking Wallula Fault Zone, NNW-striking Milton-Freewater Fault Zone, and the NNE-striking Hite Fault Zone (Hooper and Conrey, 1989; Kuehn, 1995; Hutter, 1997; Reidel and others, 2013b; Reidel and others, 2021; McClaughry and Azzopardi, 2023; Madin and others, 2023; Figures 1, 3).

The Oregon Department of Geology and Mineral Industries (DOGAMI) mapped the geology and structure of the Adams 7.5′ quadrangle between 2021 and 2024. Detailed geologic mapping of the Adams 7.5′ quadrangle is a high priority for the Oregon Geologic Map Advisory Committee because it supports long term goals for conserving and sustaining water resources, as well as reducing risks from natural hazards such as earthquakes. Our mapping was supported in part by a grant from the STATEMAP component of the U.S. Geological Survey (USGS) National Cooperative Geologic Mapping Program (NCGMP) under cooperative agreement G22AC00304. The State of Oregon provided additional funds through DOGAMI.

The chief objective of this investigation is to provide an updated and spatially accurate geologic framework for the area as part of a multiyear study of the geology of the larger Walla Walla River basin. Additional key objectives of this project are to 1) map individual CRBG lava flows and crosscutting faults to determine lava flow distribution, fault offset, fault history, and possible earthquake hazards in this part of the Walla Walla River basin of northeast Oregon, and 2) characterize the stratigraphic framework and geologic conditions controlling the distribution of water resources within the CRBG. CRBG-hosted aquifers provide a critical water supply in the map area and more widely across the Pacific Northwest (Piersol and Sprenke, 2015; Johnson and others, 2024). Textural and geochemical analysis of cuttings obtained from several water wells drilled in the greater Milton-Freewater-Athena-Adams-Helix area provides new information essential for improving interpretations of the subsurface CRBG stratigraphy and structural geology of the region (McClaughry and Azzopardi, 2023; Madin and others, 2023).

Primary map references consulted during this study include works by Hogenson (1964), Newcomb (1965), Walker (1973), Swanson and others (1981), Kuehn (1995), Hutter (1997), Ferns (2006), Ferns and Ely (2006), and Madin and Geitgey (2007). Soil information from Johnson and Makinson (1988) aided with mapping Quaternary surficial units. Additional references are cited in the Explanation of Map Units and in the DataSourcePolys feature class in the geodatabase.

The core publication products of this study are plottable geologic maps and cross sections (Plate 1), an Esri ArcGIS™ geodatabase, and Microsoft Excel® spreadsheets tabulating point data for geochemistry and well data. The geodatabase presents new geologic mapping in a digital format consistent with the USGS NCGMP Map Schema (GeMS level 3; USGS NCGMP, 2020) and contains spatial information, including map unit polygons, contacts and faults, geologic lines, geochemistry, and well data, as well as text about each geologic unit, including age, lithology, mineralogy, and structure. Surficial and bedrock units in the geodatabase are depicted on Plate 1 at a scale of 1:24,000. Plate 1 includes a detailed geologic map showing both bedrock and surficial units, including concealed bedrock contacts, and a simplified bedrock geologic map showing the distribution of contrasting bedrock lithologies and critical structural relationships. This plate (Plate 2) includes figures highlighting statewide, regional, and local structure and geologic features, tables listing select sample lab analysis, and geologic unit descriptions.

METHODS

Fieldwork for this study included collecting data along roads and conducting traverses across private lands to map lithologic contacts and faults. Geologic mapping data in the Adams 7.5′ quadrangle were collected digitally using a GPS-enabled Apple® iPad® 4 and loaded with Esri™ Collector following standard DOGAMI procedures outlined in Duda and others (2018, 2019). We used 1-meter (m) lidar digital elevation models (DEMs; 8 pts/m^2), USGS 10-m DEMs, USGS digital raster graphics of traditional topographic maps, and digital Esri™ imagery as base maps. Additionally, we recorded textural observations according to the criteria below and collected samples from different outcrops for later laboratory analysis. Volcanic rocks with fine-grained (<1 mm) average crystal or particle size in the groundmass are characterized in the following manner (Mackenzie and others, 1997; Le Maitre and others, 2002):

- As coarse groundmass if the average crystal or particle size is <1 mm and can be determined using the naked eye (>~0.5 mm)
- As medium groundmass if crystals of average size cannot be determined by eye but can be distinguished by using a hand lens (>~0.05 mm)
- As fine groundmass if crystals or grains of average size can be determined only by using a microscope or by recognition of when viewing through a hand lens of a sparkle or sheen in reflected light (indicating the presence of crystalline groundmass)
- As glassy groundmass if the groundmass has (fresh) or originally had (altered) the characteristics of glass (e.g., conchoidal fracture; sharp, transparent edges; vitreous luster)
- As intersertal if the groundmass has mixtures of crystalline and glassy characteristics; ratios of glass to crystalline materials may be indicated by textural terms including holocrystalline, hypocrystalline, hyalophitic, and holohyaline
- As containing microphenocrysts if crystals observed are larger than the overall groundmass and <1 mm across

Because many CRBG lava flows are so fine-grained and glassy, mineralogical criteria alone are insufficient to characterize these texturally similar but chemically different lava flows. As a result, whole-rock X-ray fluorescence (XRF) geochemical data are essential for separating these difficult-to-distinguish CRBG lava flows. Whole-rock geochemical samples were prepared and analyzed by XRF at the Washington State University GeoAnalytical Lab in Pullman, Washington according to Johnson and others (1999). Major element determinations are normalized to a 100 percent total on a volatile-free basis and recalculated with total iron expressed as FeOTotal (Table 1).

Chemical compositions for glass shards from tephra samples were obtained using a JEOL 8500F field emission electron microprobe at the Washington State University GeoAnalytical Lab (Table 2). Analytical results from our glass shard populations were statistically compared to a searchable reference database of western U.S. tephra compositions and ages.

To assess stream drainage morphology of secondary tributaries in the map area, we reviewed and analyzed 1-m lidar DEMs. We generated length profiles of streams from line segments with points taken every 33 m. We also generated cross-sectional profiles every 153 m from the headwaters to the intersection with the primary drainage, with generation of points along each of these cross-sectional lines every 33 m. These profiles were 305 m in length, centered on the stream center line. Finally, we evaluated cross-sectional and longitudinal profiles for all line and point features by extracting their respective elevations.

To delineate subsurface geology and the numerous concealed faults in the map area, we conducted surface-outcrop mapping, analyzed water-well logs, and interpreted high-resolution aeromagnetic data (Blakely and others, 2020a,b). Subsurface geology shown in the geologic cross sections incorporates lithologic interpretations from water-well drill records located by the Oregon Water Resources Department (OWRD) GRID system (http://apps.wrd.state.or.us/apps/gw/well_log/; Plate 1). The geodatabase includes 36 located water-well logs with interpreted subsurface geologic units. Cross section A—A′ anchors on geochemical analysis of cuttings obtained from water wells in the city Athena (e.g., UMAT 57710) and the city of Helix (e.g., UMAT 5351). Cross section B—B′ anchors on geochemical analysis of cuttings obtained from water wells in the city Athena (e.g., UMAT 57710) and the city of Adams (e.g., UMAT 5331).

To determine depth to bedrock and establish fault locations, we used 24-channel digital ReMiDAQ® seismograph-derived seismic imaging with a sampling rate of 2 milliseconds over 30-second intervals in Sand Hollow, Gerking Flat, and along Waterman Road. These surveys recorded active and ambient (passive) seismic sources. The seismic recording array consisted of 24 4.5 Hz geophones at 3.3 m spacing for a total survey length of 70 m. Active noise was generated using hammer hits during data acquisition, while ambient noise to the seismograph included nearby traffic and windmills. The recorded data were processed using Tereän's VsSurf ReMi® seismic software.

We compiled new mapping with published and unpublished data by converting it into a digital format using Esri ArcGIS™ ArcMAP™ GIS software. We created the on-screen map through heads-up digitizing using a georeferenced 1-m lidar mosaic, a 1:24,000-scale USGS DRGs of the Adams 7.5′ topographic quadrangle, and the 2020 National Agriculture Imagery Program (NAIP) digital orthophoto for Umatilla County. The geologic time scale used is the 2024 (v2024-12) version of the International Commission on Stratigraphy chronostratigraphic chart (https://stratigraphy.org/chart), revised from Gradstein and others (2004), Ogg and others (2008), and Cohen and others (2013). Colors given for hand sample descriptions are from the Geological Society of America Rock-Color Chart Committee (1991).

We used a stippled overlay on Plate 1 to show areas where sand-sized Mazama tephra is concentrated in the surface and shallow subsurface loess. These zones were identified using field observations, sample data, geochemical analyses, and interpretations of 1-m lidar topography and historic aerial photographs.

Numerical ages assigned to dated units are described in this report using standard conventions for providing ages, i.e., in terms of millions of years ago (mega-annum [Ma]) for units > 1 million years old, thousands of years ago (kilo-annum [ka]) for units < 1 million years old, and calendar years before present (B.P.) for units with reported radiocarbon ages.

STRUCTURE

Geologic structure in the Adams 7.5′ quadrangle consists of a thick section of horizontal to shallowly dipping (<1°) conformable lower to middle Miocene CRBG lava flows that are broadly folded with a wavelength of 20–23 kilometers (km). CRBG lava flows in the map area are overlain by 1—35 m of Pleistocene and Holocene loess. A network of intersecting faults crosscuts both the basalt and, locally, loess in the map area (Figure 3, Plate 1, cross sections). The axis of the broad NE-trending Agency syncline is present in the southern part of the quadrangle, where it is followed by Wildhorse Creek. The NNW-trending Waterman anticline appears in the northeast part of the map area and continues into the Waterman 7.5′ quadrangle on the north.

Three major fault zones regionally converge in this part of the Columbia Plateau, including the WNW-striking Wallula Fault Zone, NNW-striking Milton-Freewater Fault Zone, and the NNE-striking Hite Fault Zone (Hooper and Conrey, 1989; Kuehn, 1995; Hutter, 1997; Reidel and others, 2013b; Reidel and others, 2021; McClaughry and Azzopardi, 2023; Madin and others, 2023; Figures 1, 3). The Wallula Fault Zone is a set of locally active, WNW-striking right-lateral strike-slip faults and N-S-striking normal faults mapped for ~120 km from Kennewick, Washington, through Milton-Freewater, Oregon (Sherrod and others, 2016; Staisch and others, 2022). It parallels and is an integral part of the Olympic-Wallowa Lineament, an ~500-km-long collection of WNW-trending seismically active structural and physiographic features delineated between the Olympic Mountains of western Washington and the Blue Mountains of northeast Oregon (Raisz, 1945; Reidel and others, 2021). West and northwest of the Wallula Fault Zone in eastern Washington, strain is accommodated along approximately east-west-trending folds in the Yakima Fold Belt (Staisch and others, 2022; Figure 1). East of Wallula Gap (Washington), the Wallula Fault Zone transfers strain to the Hite Fault Zone across the intervening Milton-Freewater Fault Zone (Blakely and others, 2014; McClaughry and Azzopardi, 2023; Madin and others, 2023). This transition area marks the possible location of the M6 Milton-Freewater earthquake in 1936 (Blakely and others, 2014; Brocher and Sherrod, 2018). The Milton-Freewater Fault Zone is a complex zone of NNW-striking (average strike is N25°W) linear to curvilinear, vertical to subvertical, normal and/or right-lateral oblique-slip faults linking the Wallula Fault Zone on the north with the Hite Fault Zone on the southeast. Geologic mapping and review of high-resolution aeromagnetic data indicate this zone occupies an ~40-km-wide area between Wallula Gap on the west and Milton-Freewater on the east. The fault position and orientation in the map area are characteristic of Riedel shears at acute angles to the WNW-striking right-lateral strike-slip faults bracketing the Wallula Fault Zone. Normal- to right-lateral oblique-slip deformation is distributed across this structural zone. Across the ~N30°W-trending Waterman anticline, CRBG lava flows exhibit opposing structural vergence, stepping down to the west on the western limb and down to the east on the eastern limb of the fold axis (Azzopardi and others, 2023; Madin and others, 2023; Figure 3a). The Hite Fault Zone is defined by a 20- to 25-km-wide set of NNE-striking faults (average strike is N20°E), dominantly down-on-the-west, left-lateral oblique-slip faults, mapped for ~140 km between McKay Creek (OR) and Pomeroy (WA; Kienle and others, 1979; Kendall, 1981; Personius and others, 1995; Figure 3a). This zone of faulting is divided into four sections by Personius and others (1995) from northeast to southwest, including: 1) the Hite section- 2) the Kooskooskie section- 3) the Thorn Hollow section (McClaughry and Azzopardi, 2023)- and 4) the Agency section. Fault strands in the Hite fault zone are spatially coincident with and subparallel to the northeast-trending Klamath–Blue Mountain gravity-anomaly lineament, a major geophysical crustal feature recognized along the northwest slopes of the Blue Mountains (Riddihough and others, 1986; Wetzel and others, 2018; Figures 1, 3a,b).

Mapped faults in the Adams 7.5′ quadrangle all cut the middle Miocene (~14 Ma) Umatilla Member (**Tsu**) of the CRBG (Figures 2, 3a; Plate 1, cross sections). Pleistocene or possibly younger fault activity is indicated along the parallel NNW-striking Sand Hollow, Gerking Flat, and Wildhorse Creek faults, and the WNW-striking Gerking Creek quarry fault based on structural juxtaposition of loess (**Qlo**) and basalt (**Tsu**), conspicuous lineaments cutting across loess hills, and deflected stream channels. Linear geomorphic features delineating multiple strands of the Weston fault across **Qlo** mantled uplands in 1-m lidar DEMs also exhibit evidence of probable Quaternary displacement.

Milton Freewater Fault Zone

The Adams 7.5′ quadrangle includes the western part of the Milton-Freewater Fault Zone (Figure 3a) along the west limb of the Waterman anticline and includes the faults described in the section below.

Sand Hollow Fault—The Sand Hollow Fault is an entirely concealed N20°W–N30°W-striking fault parallelled by Sand Hollow in the northwest part of the map area (Plate 1, cross section A—A′). Evidence for a concealed fault includes mapped apparent normal down-on-the-southwest offset of the middle Miocene Umatilla Member (**Tsu**) and Pleistocene to Holocene loess (**Qlo**) and parallel linear NNW-trending stream drainages in the northern part of the map area paired with corresponding NNW-trending aeromagnetic lineaments (Blakely and others, 2020a,b; Figure 3b, Plate 1). The concealed fault is further resolved in an EW-trending ReMiDAQ® 2D velocity profile obtained along and parallel to Piper Road at the northern end of Sand Hollow. Here, we imaged a distinct vertical discontinuity placing **Qlo** on the west adjacent to underlying **Tsu** on the east (Figure 4a). **Tsu** crops out below several meters of **Qlo** in two places east of the Sand Hollow Fault, ~0.6 km north of Sand Hollow Road in the northwest corner of the map area and ~0.3 km east of the fault along Piper Road (see map nos. G41 and G42). The **Tsu** outcrop on Piper Road is at an elevation of 546 m. Directly east of and adjacent to the fault on Piper Road, the ReMiDAQ® 2D velocity profile indicates the top of **Tsu** is at an elevation of ~538 m in the subsurface (Figure 4a).

Tsu does not crop out west of the fault, where the top of basalt is at a comparatively lower elevation. Directly west of the fault, the ReMiDAQ® 2D velocity profile indicates ~18 m of **Qlo** overlies **Tsu** from a land surface elevation of 542 m down to a subsurface elevation of ~524 m (Figure 4a). An additional ~16 m of loess caps the ridge above this locality, indicating a cumulative **Qlo** thickness here of ~34 m. A similar thickness of **Qlo** is recognized ~1 km west of the intersection of Piper and Sand Hollow Roads. At this location, ~10 m of clay (**Qlo**) overlays basalt (**Tsu**), as revealed by water well UMAT 3039, drilled in the base of a drainage with a well-head elevation of 555 m. An additional ~25 m of **Qlo** forms the ridge above the well head, along Piper Road up to an elevation of 580 m. The vertical structural juxtaposition of middle Miocene **Tsu** and Pleistocene to Holocene **Qlo** indicates a Pleistocene or Holocene age for the latest fault offset on the Sand Hollow Fault. The ReMiDAQ® 2D velocity profile indicates 14 m of down-on-the-west vertical normal offset of the upper surface of **Tsu** across the fault (Figure 4a, Plate 1, cross section A—A′).

The Sand Hollow Fault, south of Piper Road, is also associated with steeply east-dipping **Qlo** along the western valley margin, with intercalated 7700 cal. yr B.P. Mazama tephra (Plate 1). Steep slopes of the western valley margin appear to be systematically crosscut by several inferred N45°E-striking subsidiary faults offsetting the western **Qlo**-mantled ridgeline in a left-lateral sense from north to south (Plate 1). If the steep ridges and left-lateral displaced ridge-crests are fault-related, then the latest offset along this segment of the Sand Hollow postdates deposition of the Mazama tephra and is of Holocene age.

Gerking Flat Fault—The Gerking Flat Fault is an entirely concealed N20°W-striking normal fault parallelled by Gerking Creek (Plate 1, cross section A—A′). Evidence for a concealed fault includes mapped apparent down-on-the-southwest offset of the middle Miocene Umatilla Member (**Tsu**) and Pleistocene to Holocene loess (**Qlo**) and parallel, linear NNW-trending stream drainages in the northern part of the map area paired with corresponding NNW-trending aeromagnetic lineaments (Blakely and others, 2020a,b; Figure 3, Plate 1). More details about the concealed fault emerge from an EW-trending ReMiDAQ® 2D velocity profile along and parallel to Piper Road where it crosses Gerking Creek (Figure 4b). At this location, the profile imaged a distinct vertical discontinuity, interpreted as a normal fault with ~5 m of down-on-the-west vertical offset of the bedrock surface. Bedrock here is overlain by 15–20 m of **Qlo** and **Qa**. **Tsu** crops out below several meters of **Qlo** in one location east of the Gerking Creek Fault along Gerking Flat Road (see map no. G40). It does not crop out west of the fault, where overlying loess is >30 m thick based on the ReMiDAQ® 2D velocity profile on Piper Road. The structural juxtaposition of **Tsu** and **Qlo** indicates a Late Pleistocene age for the latest fault offset on the Gerking Flat Fault.

Milton Freewater Fault Zone (continued)

Wildhorse Creek Fault—The Wildhorse Creek Fault is an entirely concealed N25°W-striking normal fault mapped beneath the unnamed NNW-trending shallow valley underlying Waterman Road between Waterman and Athena in the northeast part of the Adams 7.5′ quadrangle (Swanson and others, 1981; Figure 3, Plate 1). McClaughry and Azzopardi (2023) mapped this fault south through the Athena 7.5′ quadrangle where it is paralleled by Wildhorse and Eagle Creeks. Evidence for a concealed fault includes mapped down-on-the-west vertical offset of CRBG stratigraphy along its length, apparent vertical offset of CRBG flow stratigraphy in water wells UMAT 1462 and UMAT 57710 (Athena 7.5′ quadrangle), and a corresponding NNW-trending aeromagnetic lineament (Blakely and others, 2020a,b; McClaughry and Azzopardi, 2023; Figure 3, Plate 1). The Wildhorse Creek Fault was also recognized as a negative anomaly in high-resolution aeromagnetic data extracted along a ground transect by Staisch and others (2022) in the southern part of the Athena 7.5′ quadrangle.

McClaughry and Azzopardi (2023) used stratigraphic data from water wells UMAT 1462 and UMAT 57710 to interpret Wildhorse Creek Fault as an ~75°SW-dipping normal fault with vertical, down-on-the-southwest offset of the CRBG section. Vertical offset ranges from ~30 m in the southern part of the Athena 7.5′ quadrangle to ~60 m at the city of Athena. Between the city of Athena and Waterman, down-on-the-southwest offset of **Tsu** along the Wildhorse Creek Fault places the upper (younger) lava flow of this unit (Basalt of Sillusi) on the west against the lower (older) lava flow (Basalt of Umatilla) of the unit on the east (Figure 2, Plate 1). East of the Wildhorse Creek Fault in the northeast corner of the map area, the contact between **Tsu** and the Basalt of Sentinel Gap (**Twfsl**) is inferred and mapped at an elevation of 580 m (Figure 2, Plate 1). Just east of the fault, an outcrop of **Tsu** (lower lava flow, Basalt of Umatilla) is in the creek bottom along Waterman Road at an elevation of 570 m (Figure 2, Plate 1, map nos. G46 and G47, Table 1). **Tsu** does not crop out west of the fault. CRBG lava flows dip ~0.5° to the SSE in this area. The **Tsu**—**Twfsl** contact is at an elevation of 488 m in the city of Athena water well UMAT 57710 (McClaughry and Azzopardi, 2023). Projecting this contact up-dip to the north-northwest would place the **Tsu**—**Twfsl** contact at ~535 m elevation directly west of the Wildhorse Creek Fault (see map nos. G46 and G47). If **Tsu** is ≤10m thick directly east of the fault, then the amount of vertical down-on-the-southwest offset of the **Tsu**—**Twfsl** contact across the fault is ~20–30 m in this area. The direction and amount of vertical offset are similar to those recognized by McClaughry and Azzopardi (2023) along this fault in the Athena 7.5′ quadrangle. A Pleistocene age for the latest offset on the Wildhorse Creek Fault is indicated by the structural juxtaposition of **Tsu** and **Qlo** in the map area.

Duroc Road Fault—The Duroc Road Fault is an entirely concealed N–N10°W-striking normal fault parallelled by Duroc Road in the northwest part of the Adams 7.5′ quadrangle (Plate 1). The fault joins with or terminates against the Sand Hollow Fault at Sand Hollow (Plate 1). Evidence for a concealed fault includes the mapped apparent down-on-the-west offset of **Tsu** and the Basalt of Sand Hollow (**Twfh**) as well as the overlying **Qlo**, ~3 km north of the map area in the Waterman 7.5′ quadrangle (Guerrero and others, in press). CRBG does not crop out below **Qlo** west of the fault.

Gerking Creek Quarry Fault—The Gerking Creek Quarry Fault is an entirely concealed set of ~N50°W–N70°W-striking right-lateral strike-slip fault strands crossing Sand Hollow, Gerking Creek, and Wildhorse Creek in the central part of the Adams 7.5′ quadrangle (Plate 1, cross section B—B′). Evidence for a concealed fault includes conspicuous N70°W-striking paired lineaments recognized in 1-m lidar DEMs obliquely crossing minor drainages entrenched in unit **Qlo** between Sand Hollow and Gerking Creeks, apparent right-lateral offset of the ridgeline where the fault exits the southeast part of the quadrangle, and a WNW-trending aeromagnetic lineament paralleling these landscape features (Blakely and others, 2020a,b; Figure 3, Plate 1). Sand Hollow and Gerking Creek are both deflected in a right-lateral sense across the Gerking Creek Quarry Fault, where these drainages are crossed by OR Hwy 334. In the same area, **Tsu** is notably near the surface in the Gerking Creek quarry, where it is overlain by a comparatively thin (<1 m) layer of **Qlo** and Mazama tephra. Near-surface **Tsu** basalt here may reside in a pop-up block between two right-lateral strike-slip faults. Deflected stream drainages, fault-parallel lineaments in **Qlo**, and probable offset of the Gerking Flat Fault collectively indicate a Late Pleistocene or Holocene age for the latest fault offset on the Gerking Creek Quarry Fault.

Spring Hollow Fault—The Spring Hollow Fault is an entirely concealed ~N45°W–N65°W-striking normal fault mapped from southeast to northwest across the southern part of the Adams 7.5′ quadrangle (Figure 3, Plate 1, cross section B—B′). McClaughry and Azzopardi (2023) mapped the fault southeast through the southwest part of the Athena 7.5′ quadrangle. Northwest of the map area, the fault is concealed beneath Greasewood Creek and mapped northwest past the city of Helix. Evidence for a concealed Spring Hollow Fault in Adams 7.5′ quadrangle includes mapped apparent down-on-the-southwest offset of **Twfsl** and **Tsu** outcrops between Rainville and Spring Hollow Roads in the southeast part of the quadrangle and correspondence with a conspicuous WNW-trending aeromagnetic lineament (Blakely and others, 2020a,b; McClaughry and Azzopardi, 2023; Figure 3, Plate 1). Cross-section interpretation suggests up to 25 m of down-on-the-southwest vertical normal offset northeast of the city of Adams (McClaughry and Azzopardi, 2023; Plate 1, cross section B—B′;).

Adams Fault—The Adams Fault is an entirely concealed N50°W- to N60°W-striking normal fault mapped through the city of Adams in the southwest part of the Adams 7.5′ quadrangle (Plate 1, cross section B—B′). Evidence for a concealed fault includes mapped apparent down-on-the-northeast offset of CRBG stratigraphy and a corresponding NNW-trending aeromagnetic lineament (Blakely and others, 2020b; Figure 3, Plate 1). **Twfsl** crops out at the surface as the stratigraphically highest map unit on the north side of Wildhorse Creek along S. College Road, 0.5 km south of Adams at an elevation of 461 m (map nos. G04 and G05, Plate 1, Table 1). On the west side of the city of Adams, 0.6 km north of site G04 and G05, **Twfsl** is overlain by 32 m of **Tsu** (Basalt of Umatilla) in water well UMAT 5331 (map no. G07), placing the subsurface **Tsu**—**Twfsl** contact at an elevation of 444 m (Plate 1, cross section B—B′, Table 1). This contact relationship from south to north across the Adams Fault indicates down-on-the-northeast displacement of **Tsu**—**Twfsl** contact by ~32 m (Plate 1, cross section B—B′). The proximity of **Twfsl** surface outcrops on the south side of Adams within 0.6 km of UMAT 5331 combined with the absence of a description of broken rock (e.g., fault breccia) in the lithology log for UMAT 5331 indicates a near-vertical fault orientation (Plate 1, cross section B—B′).

Greasewood Creek Fault—The Greasewood Creek Fault is an entirely concealed ~N35°W-striking fault interpreted from a corresponding aeromagnetic lineament (Blakely and others, 2020b; Figure 3, Plate 1). The type and amount of offset and age of the latest offset along the fault is unknown (Plate 1, cross section B—B′). The southern part of this fault is likely to underlie and parallel NNW-trending Crawford Hollow in the northern part of the Cayuse 7.5′ quadrangle (Ferns, 2006); the northern part of the fault may be offset by the WNW-striking Adams Fault (Plate 1, cross section B—B′).

Weston Fault—The Weston Fault consists of a parallel set of ~N40°E striking, entirely concealed down-on-the-northwest normal faults mapped across the southeastern portion of the Adams 7.5′ quadrangle (Plate 1, cross section B—B′). Fault strand locations are interpreted from a combination of mapped vertical offset of the **Tsu**—**Twfsl** contact, distinct NE-trending topographic lineaments visible in 1-m lidar DEMs, and corresponding parallel steep magnetic gradients observed in high-resolution aeromagnetic data (Blakely and others, 2020a,b; Figure 3, Plate 1). The continuity of Weston Fault segments is disrupted from southwest to northeast, where they are offset by the NW-striking Adams, Spring Hollow, and Gerking Creek Quarry Faults (Plate 1). East of the NW-striking Wildhorse Creek Fault in the adjacent Athena 7.5′ quadrangle, McClaughry and Azzopardi (2023) mapped the Weston Fault for at least 9 km as a single ~N55°E-striking concealed and queried normal fault that trends obliquely across the NNW-striking faults of the Milton Freewater Fault Zone (Figure 3). South into the Cayuse 7.5′ quadrangle, the broadest zone of Weston fault strands aligns with and continues as a N40°E–N50°E-striking, down-on-the-northwest normal fault mapped by Ferns (2006). The cumulative offset across the fault zone is unknown. The age of the latest offset on the fault is not well-constrained, but distinct lineaments observed across **Qlo**-mantled hills in 1-m lidar DEMs suggest a probable Quaternary offset.

Interrelations between structure and geomorphology in the Adams 7.5′ quadrangle

Review and spatial analysis of 1-m lidar DEMs indicate that loess (**Qlo**)-covered areas within the Milton-Freewater Fault Zone in the Adams and adjacent Waterman, Helix, and Smeltz 7.5′ quadrangles exhibit an erosional morphology of parallel and dendritic drainage patterns distinct from the N20°E–N40°E-trending linear ridges described by Lewis (1960) for the southwestern Palouse region. The area of parallel and dendritic drainage pattern morphology lies entirely within the Milton-Freewater Fault Zone, a zone that is bounded by the Spring Hollow Fault on the west, the Gerking Creek Quarry Fault on the south, and the Wildhorse Creek Fault on the east (Figure 5). The northern limit of the area is the EW- to NWSE-trending Waterman Anticline as mapped along the uplands separating the Milton-Freewater Fault Zone on the south from the Wallula Fault Zone on the north (Guerrero and others, in press; Figures 3, 5; Plate 1).

North of the Gerking Creek Quarry Fault, 2–4-km-wide **Qlo**-mantled ridges are separated by four N20°W–N40°W-trending ~25 m deep primary alluvial valleys containing shallow intermittent streams—Greasewood Creek, Sand Hollow, Gerking Creek, and the valley beneath Waterman Road—forming prominent topographic lineaments (U.S. Geological Survey, 2022; Figure 5, Plate 1). The primary stream valleys lie directly above the concealed N20°W–N45°W-striking Spring Hollow, Sand Hollow, Gerking Flat, and Wildhorse Creek Faults (Figure 5, Plate 1). East-facing slopes with incised intermittent drainages along the western flanks of the primary stream valleys are characteristically arcuate and display steep gradients between 42 and 100 percent (Figure 5, Plate 1, cross section A—A′). Valley bottoms typically widen to the west along their length. The gently west-sloping (<5 percent) **Qlo**-mantled eastern margins of the primary valleys are less distinct. **Tsu** locally crops out beneath **Qlo** along the eastern margins of the primary stream valleys, corresponding to the upthrown blocks of NNW-striking faults, but it does not outcrop on the western margins that coincide with the downthrown blocks of these faults (Plate 1).

Between the primary stream valleys, intermittent gully drainages incise **Qlo**-mantled ridges. These incisions vary notably from parallel drainage patterns that have developed on the 1.5–2.5-km-wide western slopes and dendritic drainage patterns on the 0.5–1.5-km-wide eastern slopes (Figure 5, Plate 1). The contrasting drainage networks are separated along each ridge crest by sharp, linear, NNW-trending drainage divides. These drainage divides parallel concealed, ~N20°W- to N45°W-striking, down-on-the-west normal faults underlying the primary stream valleys (Figure 5, Plate 1).

The eastern flanks of ridges contain the thickest accumulations of Pleistocene and Holocene **Qlo** within the Adams 7.5′ quadrangle, reaching thicknesses up to 35 m (Figure 5, Plate 1). These areas of conspicuously thick **Qlo** align with dendritic networks of ~N60°E trending gullies that flow southwest to northeast and intersect the N20°W–N40°W-trending primary stream valleys nearly at right angles (Figure 5, Plate 1). Eastern ridge gullies (n = 44) average 702 m in length, have a concave length profile with an average gradient of 4.2 percent, and deep U-shaped cross-sectional profiles averaging 8 m in depth. Slopes adjacent to dendritic gullies range from 2–19 percent. Gullies along the eastern ridge flanks conspicuously contain accumulations of ~7700 cal. yr B.P. Mazama tephra above significant erosional unconformities (see the Mazama tephra overlay on Plate 1 and in the geodatabase OverlayPolys feature class, Figures 5, 6).

The western flanks of ridges contain much thinner accumulations of Pleistocene and Holocene **Qlo** and are generally less than 12 m thick within the Adams 7.5′ quadrangle. These ridge slopes drain through parallel networks of ~N20°E trending gullies that flow northeast to southwest and intersect the N20°W-trending primary stream valleys at acute angles (Figure 5, Plate 1). Western ridge gullies (n = 48) average 1,278 m in length and have a complex, convex length profile (average gradient of 3.9 percent) with gradients abruptly steepening near their confluences with the primary valleys. Cross-sectional profiles of western ridge gullies are broad and U-shaped, averaging 5 m in depth. Gully walls adjacent to western ridge gullies have comparatively gentle gradients relative to the eastern ridge gullies, ranging between 1—14 percent.

South of the Gerking Creek Quarry Fault, the **Qlo**-mantled surface is incised by Wildhorse Creek and its tributaries: Greasewood Creek, Sand Hollow, Gerking Creek, and Spring Hollow Creeks (Figure 5, Plate 1). Slopes in this part of the map area are typically less than 9 percent and few intermittent streams and gullies incise **Qlo**.

DISCUSSION

The geology and geomorphology of the Milton-Freewater Fault Zone differ notably from the surrounding region with strong evidence for a causal relationship between neotectonic activity in the area and the observed geomorphology (Figure 5). Here we present the evidence for this relationship by interpreting the relationships between bedrock and surficial units and analyzing drainage patterns on **Qlo**-mantled ridges within the Adams and surrounding Waterman, Helix, and Smeltz 7.5′ quadrangles.

Within the Milton-Freewater Fault Zone, the N20°W–N40°W-trending primary valleys and intervening **Qlo**-mantled ridges exhibit two differential patterns: parallel drainages on western flanks and dendritic drainages on eastern flanks. This configuration differs markedly from other nearby drainage patterns, including the plateaus of **Qlo** south of the Gerking Creek Quarry Fault, the minimally dissected rolling hills in the area southwest of Greasewood Creek and the Spring Hollow Fault (Helix 7.5′ quadrangle), and the linear ridge morphology of the southwestern Palouse between Helix and the Columbia River (Lewis, 1960).

The down-on-the-west Quaternary normal faults hidden beneath the main valleys of the Milton Freewater Fault Zone align with the N20°W–N40°W linear divides that separate parallel drainage on western slopes from dendritic drainage on eastern slopes (Figure 5, Plate 1). This alignment indicates that two primary controls are responsible for the contrasting drainage patterns observed across the ridges. First, regional folding and Quaternary faulting beneath the primary valleys helped establish the overall ridge valley structure and catchment orientations. Second, **Qlo** accumulated preferentially on the east facing, leeward sides of the northwest trending ridges, where prevailing southwesterly winds deposited thicker loess on the downthrown sides of the concealed faults (Figure 5, Plate 1). As a result, areas with linear, parallel drainages formed on uniform, consistently dipping slopes underlain by shallow basalt bedrock. In contrast, the dendritic drainages along the eastern flanks developed where thick accumulations of **Qlo** built up on the downthrown sides of faults hidden beneath the main valleys.

Significant erosional unconformities formed within **Qlo** on the eastern ridge flanks during the Late Pleistocene and early Holocene (Figure 6e—g). Holocene Mazama tephra accumulated to a mappable thickness where deeply incised, dendritic drainages developed within the Milton–Freewater Fault Zone (Figure 5). This thick and widespread accumulation of Mazama tephra contrasts markedly with the **Qlo** mantled, minimally dissected rolling hills southwest of Greasewood Creek and the Spring Hollow Fault in the Helix 7.5′ quadrangle where similar Mazama tephra deposits are uncommon.

Pleistocene and younger faulting similar to that observed in the study area has been mapped along the Wallula Fault Zone in the adjacent Waterman 7.5′ quadrangle to the north (Guerrero and others, in press). This segment of the Wallula Fault Zone coincides with the proposed epicenter for the 1936 M6 Milton-Freewater earthquake, the largest historic earthquake recorded in the region (Blakely and others, 2014; Brocher and Sherrod, 2018).

ACKNOWLEDGMENTS

Geologic mapping in the Adams 7.5′ quadrangle was supported through the STATEMAP component of the U.S. Geological Survey National Cooperative Geologic Mapping Program under cooperative agreement G22AC00304. Additional funding was provided by the State of Oregon through DOGAMI. Dr. Ashley Steiner and Dr. Scott Boroughs at the GeoAnalytical lab at Washington State University, respectively prepared and analyzed geochemical samples by XRF and tephra samples by Electron Microprobe. Vanessa Swenton (DOGAMI) constructed the water well feature class. Cartography for the map plates was done by Jon Franczyk (DOGAMI). Kellum Tate-Jones (DOGAMI) provided editing, formatted the final publication, and developed the webpage. Critical and insightful reviews by Mark Ferns (DOGAMI-retired), Jen Woody (OWRD), Ian Yuh (USGS), and Reed Burgette (DOGAMI) greatly enriched the final publication.

REFERENCES

Angster, S.J., Sherrod, B.L., and Lasher, J., 2023, Logs and data from thBacon C.R., 1983, Eruptive history of Mount Mazama and Crater Lake Caldera, Cascade Range, U.S.A.: Journal of Volcanology and Geothermal Research, v. 18, no. 1–4, p. 57–115, https://www.sciencedirect.com/science/article/abs/pii/0377027383900045, accessed December 16, 2025.

Bacon, C.R., 2008, Geologic map of Mount Mazama and Crater Lake Caldera, Oregon: U.S. Geological Survey Scientific Investigations Map 2832, 4 sheets, scales 1:24,000 and 1:50,000, 45 p., https://pubs.usgs.gov/sim/2832/, accessed December 16, 2025.

Bacon C.R. and Lanphere M.A., 2006, Eruptive history and geochronology of Mount Mazama and the Crater Lake region, Oregon: Geological Society of America Bulletin, v. 118, no. 11–12, p. 1331–1359, https://pubs.geoscienceworld.org/gsa/gsabulletin/article-abstract/118/11-12/1331/519053/Eruptive-history-and-geochronology-of-Mount-Mazama?redirectedFrom=fulltext, accessed December 16, 2025.

Bacon, C.R., and Wright, H.M., 2017, Geologic field trip guide to Mount Mazama and Crater Lake Caldera, Oregon: U.S. Geological Survey Scientific Investigations Report 2017–5022–J1, 47 p., https://doi.org/10.3133/sir20175022J1, accessed December 16, 2025.

Baker, V.R., 2009, The channeled scabland: A retrospective: Annual Review of Earth and Planetary Science v. 37, p. 393-411, https://www.annualreviews.org/content/journals/10.1146/annurev.earth.061008.134726, accessed January 14, 2026.

Baksi, A.K., 2022, New 40Ar/39Ar ages from the Grande Ronde and Wanapum Basalt, Columbia River Basalt Group (CRBG): Compilation of all ages and relationship to the geomagnetic polarity time scale for ~17–15 Ma: Journal of Earth System Science, v. 131 158, p. 1-29, https://www.ias.ac.in/article/fulltext/jess/131/0158, accessed December 16, 2025.

REFERENCES (continued)

Barry, T.L., Kelley, S.P., Reidel, S.P., Camp, V.E., Self, S., Jarboe, N.A., Duncan, R.A., and Renne, P.R., 2013, Eruption chronology of the Columbia River Basalt Group, in Reidel, S.P., Camp, V.E., Martin, M.E., Ross, M.E., Wolff, J.A., Martin, B.S., Tolan, T.L., and Wells, R.E., eds., The Columbia River Flood Basalt Province: Geological Society of America Special Paper 497, p. 45–66, https://pubs.geoscienceworld.org/books/book/661/chapter/3807104/Eruption-chronology-of-the-Columbia-River-Basalt , accessed December 16, 2025.

Blakely, R.J., Sherrod, B.L., Weaver, C.S., Wells, R.E., and Rohay, A.C., 2014, The Wallula fault and tectonic framework of south-central Washington, as interpreted from magnetic and gravity anomalies: Tectonophysics, v. 624, p. 32-45, https://www.sciencedirect.com/science/article/abs/pii/S0040195113006501?via%3Dihub, accessed December 16, 2025.

Blakely, R.J., and Sherrod, B.L. and Weaver, C.S., 2020a, High-Resolution Aeromagnetic Survey of the Pasco Area, Washington and Oregon: U.S. Geological Survey data release, https://doi.org/10.5066/P96U1HY0, accessed December 16, 2025.

Blakely, R.J., Sherrod, B.L., Glen, J.M., Ritzinger, B.T., and Mills, P.F., 2020b, High-Resolution Aeromagnetic Survey Over Pendleton, Oregon, and Surrounding Areas: U.S. Geological Survey data release, https://doi.org/10.5066/P9V23JA6, accessed December 16, 2025.

Bjornstad, B.N., Fecht, K.R., Pluhar, C.J., 2001, Long history of pre-Wisconsin, ice age cataclysmic floods: evidence from southeastern Washington state: Journal of Geology, v. 109, no. 6, p. 695–713, https://www.journals.uchicago.edu/doi/10.1086/323190, accessed December 16, 2025.

Brocher T.M., and Sherrod B.L., 2018, Intensities, Aftershock Sequences, and the Location of the 1936 Milton-Freewater Earthquake near the Oregon–Washington Border, U.S.A.: Bulletin of the Seismological Society of America, v. 108, p. 2594-2613, https://pubs.geoscienceworld.org/ssa/bssa/article-abstract/108/5A/2594/547752/Intensities-Aftershock-Sequences-and-the-Location, accessed December 16, 2025.

Busacca, A.J., 1989, Long Quaternary record in eastern Washington, U.S.A., interpreted from multiple buried paleosols in loess: Geoderma, v. 45, 105e122, https://www.sciencedirect.com/science/article/abs/pii/0016706189900451, accessed December 16, 2025.

Bush, J. H., Jr., Morton, J. A., Anderson, J. V., Crosby, J. W., III, and Siems, B. A., 1973, Test-observation well near Walla Walla, Washington—Description, stratigraphic relationships and preliminary results: Washington State University College of Engineering Research Division Research Report 73/15-66, 1 v.

Cahoon, E.B., Streck, M.J., Koppers, A.A.P., and Miggins, D.P., 2020, Reshuffling the Columbia River Basalt chronology—Picture Gorge Basalt, the earliest- and longest-erupting formation: Geology, v. 48, p. 348-352, https://doi.org/10.1130/G47122.1, accessed December 16, 2025.

Cahoon, E.B., Streck, M.J., Koppers, A.A.P., 2023, Picture Gorge Basalt: Internal stratigraphy, eruptive patterns, and its importance for understanding Columbia River Basalt Group magmatism: Geosphere, v. 19, no. 2, p 406–430, https://pubs.geoscienceworld.org/gsa/geosphere/article/19/2/406/620369/Picture-Gorge-Basalt-Internal-stratigraphy, accessed December 16, 2025.

Cohen, K.M., Finney, S.C., Gibbard, P.L., and Fan, J.X., 2013 (updated 2015), The ICS International Chronostratigraphic Chart: Episodes 36, p. 199-204, https://stratigraphy.org/chart#latest-version, accessed December 16, 2025.

Darin, M.H., McClaughry, J.D., Azzopardi, C.J.M., Franczyk, J. J., and Madin, I.P., 2025, Oregon Geologic Data Compilation, release 8 [OGDC-8] (statewide): Oregon Department of Geology and Mineral Industries Digital Data Series OGDC-8 (supersedes all previous releases of OGDC), 15 p., Esri geodatabase (GeMS), metadata, https://www.oregon.gov/dogami/pubs/Pages/dds/p-OGDC-8.aspx, accessed December 16, 2025.

Dicken, S.N., 1965, Oregon Geography: The people, the place, and the time, 4th ed: Ann Arbor, Mich., Edwards Brothers, 147 p.

Duda, C.J.M., McClaughry, J.D., Houston, R.A., and Niewendorp, C.A., 2018, Lidar and Structure from Motion-enhanced geologic mapping, examples from Oregon, in Thorleifson, L. H., ed., 2018, Geologic Mapping Forum 2018 Abstracts: Minnesota Geological Survey Open File Report OFR-18-1, 107 p., https://conservancy.umn.edu/handle/11299/194852, accessed December 16, 2025.

Duda, C.J.M., McClaughry, J.D., and Madin, I.P., 2019, Building the modern geologic map in Oregon: a multi-faceted field- and technology-based approach: Geological Society of America Abstracts with Programs, v. 51, no. 4, https://gsa.confex.com/gsa/2019CD/meetingapp.cgi/Paper/329552, accessed December 16, 2025.

Egan, J., Blackford, J.J., and Staff, R.A., 2015, A high-precision age estimate of the Holocene Plinian eruption of Mount Mazama, Oregon, USA: The Holocene, v. 25, no. 7, p. 1-14, https://journals.sagepub.com/doi/abs/10.1177/0959683615576230?journalCode=hola, accessed December 16, 2025.

Ferns, M.L., 2006, Preliminary geologic map of the Cayuse 7.5 minute quadrangle: Oregon Department of Geology and Mineral Industries Open-File Report O-06-08, 1 plate, scale 1:24,000, 9 p., https://pubs.oregon.gov/dogami/ofr/O-06-08.zip, accessed December 16, 2025.

Ferns, M.L., and Ely, K., 2006, Preliminary geologic map of the Mission 7.5 minute quadrangle: Oregon Department of Geology and Mineral Industries Open-File Report O-06-09, 1 plate, scale 1:24,000, 11 p., https://pubs.oregon.gov/dogami/ofr/O-06-09.zip, accessed December 16, 2025.

Ferns, M.L., and McClaughry, J.D., 2013, Stratigraphy and volcanic evolution of the middle Miocene La Grande–Owyhee eruptive axis in eastern Oregon, in Reidel, S.P., Camp, V. Ross, M.E., Wolff, J.A., Martin, B.E., Tolan, T.L., and Wells, R.E., eds., The Columbia River Flood Basalt Province: Geological Society of America Special Paper 497, p. 401-427, https://pubs.geoscienceworld.org/books/book/661/chapter-abstract/3807352/Stratigraphy-and-volcanic-evolution-of-the-middle?redirectedFrom=fulltext, accessed December 16, 2025.

Ferns, M.L., McConnell, V.S., Madin, I.P., and Johnson, J.A., 2010, Geology of the Upper Grande Ronde River Basin, Union County, Oregon: Oregon Department of Geology and Mineral Industries Bulletin 107, 65 p., 1 plate, scale 1:100,000, Esri™ format shapefiles, dbf files; spreadsheet (5 sheets), geo-located photographs (19), https://pubs.oregon.gov/dogami/B/p-B-107.htm, accessed December 16, 2025.

Geological Society of America Rock-Color Chart Committee, 1991, Rock color chart, 7th printing: Boulder, CO.

Gradstein, F.M., Ogg, J.A., and Smith, A., G., 2004, A Geologic Time Scale 2004, Cambridge University Press, 589 p.

Guerrero, E.F., McClaughry, J.D., Azzopardi, C.J.M., Gaylord, D.R., Anthony, L.H., Walker, R.J., Swenton, V.M., and Burgette, R.J., in press, Geologic map of the Waterman 7.5′ quadrangle, Umatilla County, Oregon: Oregon Department of Geology and Mineral Industries Geologic Map Series GMS 13X, 2 plates, scale 1:24,000, Esri format geodatabase; shapefiles; metadata, https://pubs.oregon.gov/dogami/gms/p-GMS-13X.htm, accessed January 31, 2026.

Herrero-Bervera, E., C. E. Helsley, A. M. Sarna-Wojcicki, K. R. Lajoie, C. E. Meyer, M. O. McWilliams, R. M. Negrini, B. D. Turrin, J. M. D. Nolan, and J. C. Liddicoat, 1994, Age and correlation of a paleomagnetic episode in the western United States by $^{40}Ar/^{39}Ar$ dating and tephrochronology: The Jamaica, Blake, or a new polarity episode?: Journal of Geophysical Research, v. 99(B12), p. 24091–24103, https://agupubs.onlinelibrary.wiley.com/doi/10.1029/94JB01546, accessed December 16, 2025.

Hogenson, G.M., 1964, Geology and ground water of the Umatilla River basin, Oregon: U.S. Geological Survey Water Supply Paper 1620, 162 p., https://pubs.er.usgs.gov/publication/wsp1620, accessed December 16, 2025.

Hooper, P.R., 2000, Chemical discrimination of Columbia River Basalt flows: Geochemistry, Geophysics, and Geosystems, v. 1, no. 1, p. 1-14, https://onlinelibrary.wiley.com/doi/10.1029/2000GC000040/pdf, accessed December 16, 2025.

Hooper, P.R., and Conrey, R.M., 1989, A model for the tectonic setting of the Columbia River basalt eruptions, in Reidel, S.P., and Hooper, P.R., eds., Volcanism and tectonism in the Columbia River flood-basalt province: Geological Society of America Special Paper 239, p. 293-306, https://pubs.geoscienceworld.org/gsa/books/book/375/Volcanism-and-Tectonism-in-the-Columbia-River, accessed December 16, 2025.

Hutter, I. L., 1997, The Wallula Fault Zone: A study of the structure and tectonic history of a portion of the Olympic-Wallowa Lineament: Bellingham, Western Washington University, M.S. thesis, 194 p.

Johnson, D.M., Hooper, P.R., and Conrey, R.M., 1999, XRF analysis of rocks and minerals for major and trace elements on a single low dilution Li-tetraborate fused bead: Advances in X-ray Analysis, v. 41, p. 843-867, https://s3.wp.wsu.edu/uploads/sites/2191/2017/06/Johnson-Hooper-and-Conrey.pdf, accessed December 16, 2025.

Johnson, D.R., and Makinson, A.J., 1988, Soil survey of Umatilla County Area, Oregon: Natural Resources Conservation Service Soil Conservation Survey 667, 388 p., https://nrcs.app.box.com/s/taycqfsrlbxjocs6ck4a68y96gqsvd76/file/982604665170, accessed December 16, 2025.

Johnson, H.M., Ely, K., and Maher, A., 2024, Timing and source of recharge to the Columbia River Basalt Groundwater System in Northeast Oregon: Groundwater, v. 62, no. 5, p 761-777., https://ngwa.onlinelibrary.wiley.com/doi/10.1111/gwat.13404, accessed December 16, 2025.

Kasbohm, J., and Schoene, B., 2018, Rapid eruption of the Columbia River flood basalt and correlation with mid-Miocene climate optimum; Science Advances, v. 4, no. 9, https://advances.sciencemag.org/content/4/9/eaat8223, accessed December 16, 2025.

Kasbohm, J., Schoene, B., Mark, D.F., Murray, J., Reidel, S., Szymanowski, D., Barfod, D., Barry, T., 2023, Eruption history of the Columbia River Basalt Group constrained by high-precision U-Pb and $^{40}Ar/^{39}Ar$ geochronology: Earth and Planetary Science Letters, Volume 617, p. 1-14, https://www.sciencedirect.com/science/article/abs/pii/S0012821X23002820, accessed December 16, 2025.

Kendall, J.J., 1981, The geology and structure of the Blue Mountains in northeastern Umatilla County, Oregon: Los Angeles, University of Southern California, M.S. Thesis, 103 p.

Kienle, C.F., Jr., Hamill, M.L., and Clayton, D.N., 1979, Geological Reconnaissance of the Wallula Gap Washington - Blue Mountains - La Grande, Oregon region: Unpublished report prepared for the Washington Public Power Supply System by Shannon and Wilson Inc., contract no. 44013, C.O. No 38, 58 p.

Kuehn, S. C., 1995, The Olympic-Wallowa Lineament, Hite Fault System, and Columbia River Basalt Group Stratigraphy in northeast Umatilla County, Oregon: Pullman, Washington State University, M.S. Thesis, 170 p.

Laval, W.N., 1956, Stratigraphy and Structural Geology of Portions of South-Central Washington: Ph.D. dissertation, Seattle, University of Washington, 208 p.

Le Maitre, R.W. (ed.), Streckeisen, A., Zanettin, B., Le Bas, M.J,, Bonin, B., and Bateman, P., 2002, Igneous rocks: A classification and glossary of terms: Second Edition, Cambridge University Press, Recommendations of the International Union of Geological Sciences, Subcommission on the Systematics of Igneous Rocks, 236 p., https://doi.org/10.1017/CBO9780511535581, accessed December 16, 2025.

Lewis, P.F., 1960, Linear topography in the southwestern Palouse, Washington-Oregon: Annals of the Association of American Geographers, v. 50, no. 2, p98-111.

Mackenzie, W.S., Donaldson, C.H., and Guilford, C., 1997, Atlas of igneous rocks and their textures: Addison Wesley Longman Ltd., 7th ed., 148 p.

Madin, I.P., and Geitgey, R.P., 2007, Preliminary geologic map of the Umatilla Basin, Morrow and Umatilla Counties, Oregon: Oregon Department of Geology and Mineral Industries Open-File Report O-07-15, 3 plates, scale 1:100,000, https://pubs.oregon.gov/dogami/ofr/O-07-15.zip, accessed December 16, 2025.

Madin, I.P., McClaughry, J.D., and Azzopardi, C.J.M., 2023, Geologic map of the Milton-Freewater and Bowlus Hill 7.5′ quadrangles: Oregon Department of Geology and Mineral Industries Geological Map Series GMS 130, 2 map plates (scale 1:24,000), plate of cross sections, and plate of explanatory text, Esri format geodatabase (GeMS level 3), shapefiles, metadata, spreadsheets (16 sheets). https://www.oregon.gov/dogami/pubs/Pages/gms/p-GMS-130.aspx, accessed December 16, 2025.

Mahood, G.A., and Benson, T.R., 2017, Using $^{40}Ar/^{39}Ar$ ages of intercalated silicic tuffs to date flood basalts: Precise ages for Steens Basalt Member of the Columbia River Basalt Group: Earth and Planetary Science Letters, v. 459, p. 340-351, https://www.sciencedirect.com/science/article/abs/pii/S0012821X16306720?via%3Dihub, accessed December 16, 2025.

McClaughry, J.D., and Azzopardi, C.J.M., 2023, Geologic map of the Athena 7.5′ quadrangle, Umatilla County, Oregon: Oregon Department of Geology and Mineral Industries Geologic Map Series GMS 129, 2 plates, scale 1:24,000, Esri format geodatabase; shapefiles; metadata, https://pubs.oregon.gov/dogami/gms/p-GMS-129.htm, accessed December 16, 2025.

McDonald, E.V., and Busacca, A.J., 1988, Record of pre-late Wisconsin giant floods in the Channeled Scabland interpreted from loess deposits: Geology, v. 16, no. 8, p. 728-731, https://pubs.geoscienceworld.org/gsa/geology/article-abstract/16/8/728/204738/Record-of-pre-late-Wisconsin-giant-floods-in-the, accessed December 16, 2025.

McDonald, E.V., Sweeney, M.R., and Busacca, A.J., 2012, Glacial outburst floods and loess sedimentation documented during Oxygen Isotope Stage 4 on the Columbia Plateau, Washington State: Quaternary Science Reviews v. 45, p. 18-30, https://www.sciencedirect.com/science/article/abs/pii/S0277379112001412, accessed December 16, 2025.

Moore, N.E., Grunder, A.L., and Bohrson, W.A., 2018, The three-stage petrochemical evolution of the Steens Basalt (southeast Oregon, USA) compared to large igneous provinces and layered mafic intrusions: Geosphere, v. 14, p. 2505-2532, https://pubs.geoscienceworld.org/gsa/geosphere/article/14/6/2505/548601/The-three-stage-petrochemical-evolution-of-the, accessed December 16, 2025.

Newcomb, R.C., 1965, Geology and groundwater resources of the Walla Walla River basin, Washington-Oregon: Washington Division of Water Resources Water Supply Bulletin 21, 151 p., https://apps.ecology.wa.gov/publications/summarypages/wsb21.html, accessed December 16, 2025.

Nersinger, R.M., 2021, The Umatilla Member of the Columbia River Basalt Group, a chemically unusual flood basalt: Pullman, Washington State University, M.S. Thesis, 96 p.

Ogg, J.G., Ogg, G., and Gradstein, F.M., 2008, Concise geologic time scale. Cambridge, University Press, 177.

Patton, P.C., Baker, V.R., 1978, New evidence for pre-Wisconsin flooding in the channeled scabland of eastern Washington: Geology v. 6, p. 567-571, https://pubs.geoscienceworld.org/gsa/geology/article-abstract/6/9/567/190155/New-evidence-for-pre-Wisconsin-flooding-in-the, accessed January 14, 2026.

Personius, S.F., Dart, R.L., Bradley, L.A., and Haller, K.M., 1995, Map and data for Quaternary faults and folds in Oregon: U.S. Geological Survey Open-File Report 03-095, 556 p., https://pubs.usgs.gov/of/2003/ofr-03-095/OFR_03_095_text.pdf, accessed December 16, 2025.

Piersol, M.W., and Sprenke, K.F., 2015, A Columbia River Basalt Group Aquifer in sustained drought: Insight from Geophysical Methods: Resources, v. 4., p. 557-596, https://www.mdpi.com/2079-9276/4/3/577, accessed December 16, 2025.

Pluhar, C.J., Bjornstad, B.N., Reidel, S.P., Coe, R.S., and Nelson, P.B., 2006, Magnetostratigraphic evidence from the Cold Creek bars for onset of ice-age cataclysmic floods in eastern Washington during the Early Pleistocene: Quaternary Research, v. 65, p.123-135, https://www.sciencedirect.com/science/article/abs/pii/S0033589405000979, accessed December 16, 2025.

Raisz, E., 1945, The Olympic-Wallowa Lineament: American Journal of Science, v. 243-A, p. 479-485.

Reidel, S.P., and Tolan, T.L., 2013, The Grande Ronde Basalt, Columbia River Basalt Group, in Reidel, S.P., Camp, V.E., Martin, M.E., Ross, M.E., Wolff, J.A., Martin, B.S., Tolan, T.L., and Wells, R.E., eds., The Columbia River Flood Basalt Province: Boulder, Colorado, Geological Society of America Special Paper 497, p. 117-154, https://pubs.geoscienceworld.org/books/book/661/chapter-abstract/3807152/The-Grande-Ronde-Basalt-Columbia-River-Basalt?redirectedFrom=fulltext, accessed December 16, 2025.

Reidel, S.P., Johnson, V.G., and Spane, F.A., 2002, Natural gas storage in basalt aquifers of the Columbia Laboratory, Basin, Pacific Northwest USA: a guide to site characterization: Richland, Wash., Pacific Northwest National 277 p., https://www.pnnl.gov/main/publications/external/technical_reports/PNNL-13962.pdf, accessed December 16, 2025.

Reidel, S.P., Camp, V.E., Tolan, T,L., and Martin, B.S., 2013a, The Columbia River flood basalt province: Stratigraphy, aerial extent, volume, and physical volcanology, in Reidel, S.P., Camp, V.E., Martin, M.E., Ross, M.E., Wolff, J.A., Martin, B.S., Tolan, T.L., and Wells, R.E., eds., The Columbia River Flood Basalt Province: Boulder, Colorado, Geological Society of America Special Paper 497, p. 1-43, https://pubs.geoscienceworld.org/books/book/661/chapter-abstract/3807083/The-Columbia-River-flood-basalt-province?redirectedFrom=fulltext, accessed December 16, 2025.

Reidel, S.P., Camp, V.E., Tolan, T.L., Kauffman, J.D., and Garwood, D.L., 2013b, Tectonic evolution of the Columbia River flood basalt province, in Reidel, S.P., Camp, V.E., Martin, M.E., Ross, M.E., Wolff, J.A., Martin, B.S., Tolan, T.L., and Wells, R.E., eds., The Columbia River Flood Basalt Province: Boulder, Colorado, Geological Society of America Special Paper 497, p. 293-324, https://pubs.geoscienceworld.org/books/book/661/chapter-abstract/3807278/Tectonic-evolution-of-the-Columbia-River-flood?redirectedFrom=fulltext, accessed December 16, 2025.

Reidel, S.P., Fecht, K.R., Hutter (Harrold) I.L., Tolan, T., and Chamness, M.A., 2021, The Olympic-Wallowa lineament: A new look at an old controversy: Geological Society of America Bulletin, v. 133, p. 115-133, https://pubs.geoscienceworld.org/gsa/gsabulletin/article-abstract/133/12/115/586095/The-Olympic-Wallowa-lineament-A-new-look-at-an-old?redirectedFrom=fulltext, accessed December 16, 2025.

Riddihough, R., Finn, C., and Couch, R., 1986, Klamath–Blue Mountain lineament, Oregon: Geology, v. 14, p. 528–531, https://pubs.geoscienceworld.org/gsa/geology/article-abstract/14/6/528/204089/Klamath-Blue-Mountain-lineament-Oregon, accessed December 16, 2025.

Seims, B.A., Bush, J.G., and Crosby, J.W. III, 1974, TiO_2 and geophysical logging criteria for Yakima Basalt correlation, Columbia Plateau: Geological Society of America Bulletin, v. 85, 1061-1068, https://pubs.geoscienceworld.org/gsa/gsabulletin/article-abstract/85/7/1061/201633/TiO2-and-Geophysical-Logging-Criteria-for-Yakima, accessed December 16, 2025.

Sherrod, B.L., Blakely, R.J., Lasher, J.P., Lamb, A., Mahan, S.A., Foit, F.F., Jr., and Barnett, E.A., 2016, Active faulting on the Wallula fault zone within the Olympic-Wallowa lineament, Washington State, USA: Geological Society of America Bulletin, v. 128, p. 1639-1659, https://pubs.geoscienceworld.org/gsa/gsabulletin/article/128/11-12/1636/185319/Active-faulting-on-the-Wallula-fault-zone-within, accessed December 16, 2025.

Staisch, L.M., Angster, S., Bennett, S.E.K., Blakely, R,J., Sherrod, B., Stephenson, W., and Lasher, J., 2022, Geomorphology, geophysics, and geology along the Wallula fault zone, Washington and Oregon: Geological Society of America Abstracts with Programs. v. 54, no. 5, https://gsa.confex.com/gsa/2022AM/webprogram/Paper381799.html, accessed December 16, 2025.

Stuiver, Minze, Reimer, P.J., and Braziunas, T.F., 1998, High-precision radiocarbon age calibration for terrestrial and marine samples: Radiocarbon, v. 40, p. 1127–1151, https://www.cambridge.org/core/journals/radiocarbon/article/highprecision-radiocarbon-age-calibration-for-terrestrial-and-marine-samples/1660E9D7A43772ACBB56614C1DD09D46, accessed December 16, 2025.

Swanson, D.A., Wright, T.L., Hooper, P.R., and Bentley, R.D., 1979, Revisions in stratigraphic nomenclature of the Columbia River Basalt Group: U.S. Geological Survey Bulletin 1457-G, 59 p., 1 pl., https://pubs.er.usgs.gov/publication/b1457G, accessed December 16, 2025.

Swanson, D.A., Anderson, J.A., Camp, V.E., Hooper, P.R., Taubeneck, W.H., and Wright, T.L., 1981, Reconnaissance geologic map of the Columbia River Basalt Group, Northern Oregon and Western Idaho: U.S. Geological Survey Open-File Report 81-797, 35 p., 6 pl., scale 1:250,000, https://pubs.er.usgs.gov/publication/ofr81797, accessed December 16, 2025.

Tolan, T.L., Lindsey, K.A., and Reidel, S.P., 2009, Stratigraphy and structure of the Columbia River Basalt Group beneath the Walla Walla Basin, Washington and Oregon: Geological Society of America Abstracts with Programs, v. 41, no. 7, p. 225.

U.S. Energy Research and Development Administration, 1976, Preliminary Feasibility Study on Storage of Radioactive Waste in Columbia River Basalts: U.S. Energy Research and Engineering Division Report ARH-ST-137 under contract E(45-1)-2130, 183 p.

U.S. Geological Survey National Cooperative Geologic Mapping Program, 2020, GeMS (Geologic Map Schema)—A standard format for the digital publication of geologic maps: U.S. Geological Survey Techniques and Methods, book 11, chap. B10, 74 p. https://doi.org//10.3133/tm11B10, accessed December 16, 2025.

U.S. Geological Survey, 2022, National Hydrography Dataset Plus High Resolution [Data set]: https://www.usgs.gov/national-hydrography

Waitt, R.B., 1985, Case for periodic, colossal jökulhlaups from Pleistocene glacial Lake Missoula: Geological Society of America Bulletin 96, p. 1271-1286, https://pubs.geoscienceworld.org/gsa/gsabulletin/article-abstract/96/10/1271/202979/Case-for-periodic-colossal-jo-kulhlaups-from, accessed January 14, 2026.

Walker, G. W., 1973, Reconnaissance geologic map of the Pendleton quadrangle, Oregon and Washington: U.S. Geological Survey Miscellaneous Geologic Investigations Map I-727, scale 1:250,000, https://pubs.er.usgs.gov/publication/i727, accessed December 16, 2025.

Washington Geological Survey, Geologic provinces of Washington, https://www.dnr.wa.gov/programs-and-services/geology/explore-popular-geology/geologic-provinces-washington, accessed December 16, 2025.

Wetzel, K.F., Bennett, S.E.K., Staisch, L., Blakely, R.J., Lamb, A.P., and Earney, T., 2018, Field geophysical investigations of the Blue Mountains uplift, northeastern Oregon: American Geophysical Union, Fall Meeting 2018, abstract #T51G-0250, https://ui.adsabs.harvard.edu/abs/2018AGUFM.T51G0250W/abstract, accessed December 16, 2025.

Zdanowicz, C.M., Zielinski, G.A., and Germani, M.S., 1999, Mount Mazama eruption—Calendrical age verified and atmospheric impact assessed: Geology, v. 27, p. 621–624, https://pubs.geoscienceworld.org/gsa/geology/article-abstract/27/7/621/189526/Mount-Mazama-eruption-Calendrical-age-verified-and?redirectedFrom=fulltext, accessed December 16, 2025.

NOTICE: This manuscript is submitted for publication with the understanding that the United States Government is authorized to reproduce and distribute reprints for governmental use. The views and conclusions contained in this document are those of the authors and should not be interpreted as necessarily representing the official policies, either expressed or implied, of the U.S. government.

This product is for informational purposes and may not have been prepared for or be suitable for legal, engineering, or surveying purposes. Users of this information should review or consult the primary data and information sources to ascertain the usability of the information. This publication cannot substitute for site-specific investigations by qualified practitioners. Site-specific data may give results that differ from the results shown in the publication.

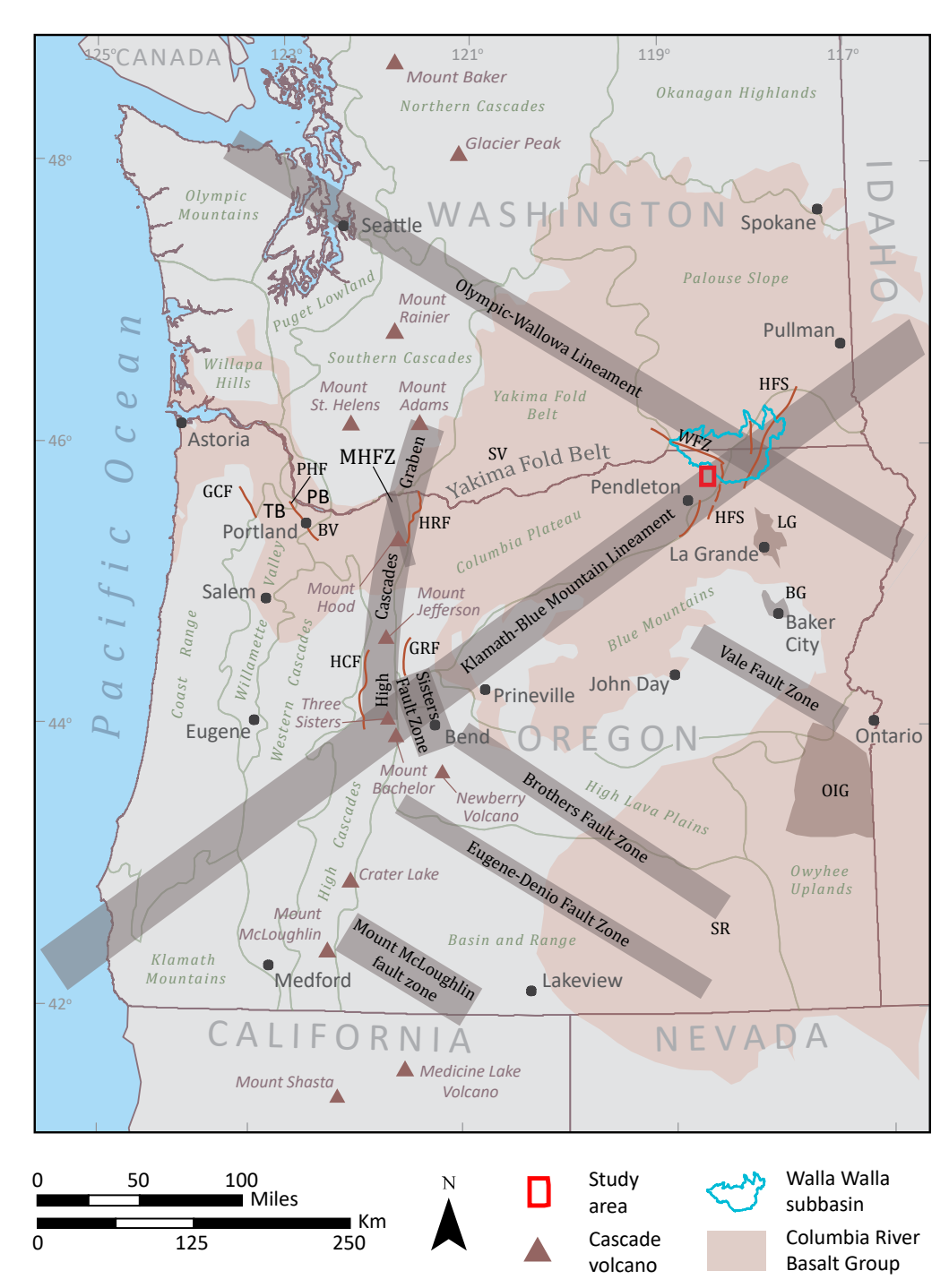

Figure 1. Map highlighting selected major volcanic and structural features in Oregon. The extent of the Walla Walla River basin outlined with a light blue line; red polygon shows the boundaries of the Adams 7.5′ quadrangle. The light brown shading corresponds with the outcrop distribution of the CRBG, including areas from which the lava flows have been eroded, as well as to areas where lava flows are concealed by younger units. Modified from Reidel and others (2013a) and Ferns and McClaughry (2013). Labels: BG – Baker graben; BV – Boring Volcanic Field; HFS – Hite fault zone; HRF – Hood River fault zone; HCF – Horse Creek fault zone; GCF – Gales Creek fault; GRF – Green Ridge fault zone; LG – La Grande graben; OIG – Oregon-Idaho graben; PB – Portland Basin; PHF – Portland Hills fault; MHFZ – Mount Hood fault zone; SR – Steens Ridge; SV – Simcoe Mountains Volcanic Field; TB – Tualatin Basin; WFZ – Wallula fault zone. Oregon physiographic provinces after Dicken (1965). Washington physiographic provinces are from Washington Department of Natural Resources.

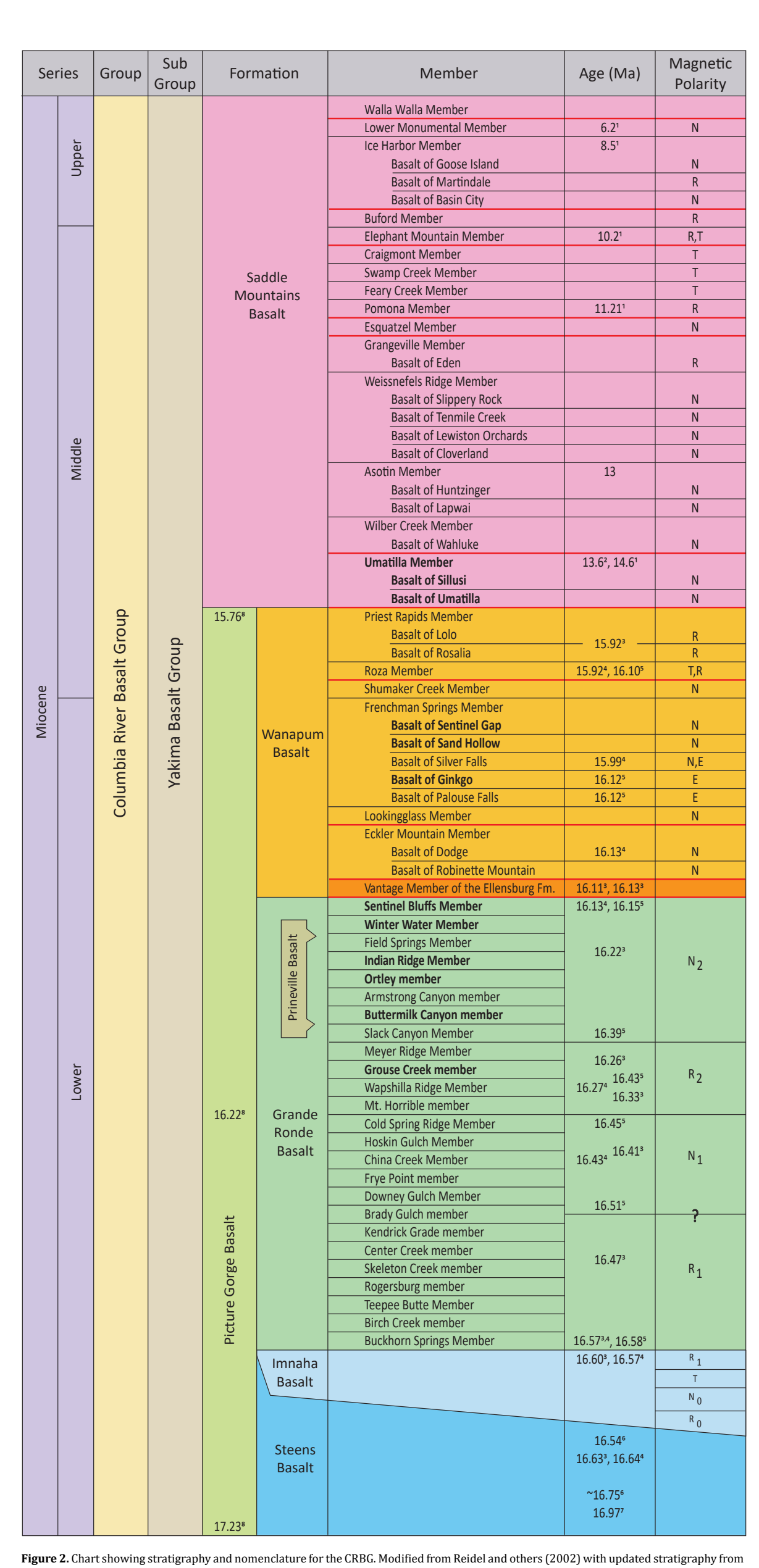

Series		Group	Sub Group	Formation		Member	Age (Ma)	Magnetic Polarity
Miocene	Upper	Columbia River Basalt Group	Yakima Basalt Group		Saddle Mountains Basalt	Walla Walla Member		
						Lower Monumental Member	6.2[1]	N
						Ice Harbor Member	8.5[1]	
						Basalt of Goose Island		N
						Basalt of Martindale		R
						Basalt of Basin City		N
						Buford Member		R
	Middle					Elephant Mountain Member	10.2[1]	R,T
						Craigmont Member		T
						Swamp Creek Member		T
						Feary Creek Member		T
						Pomona Member	11.21[1]	R
						Esquatzel Member		N
						Grangeville Member		
						Basalt of Eden		R
						Weissenfels Ridge Member		
						Basalt of Slippery Rock		N
						Basalt of Tenmile Creek		N
						Basalt of Lewiston Orchards		N
						Basalt of Cloverland		N
						Asotin Member	13	
						Basalt of Huntzinger		N
						Basalt of Lapwai		N
						Wilber Creek Member		
						Basalt of Wahluke		N
						Umatilla Member	13.6[2], 14.6[1]	
						Basalt of Sillusi		N
						Basalt of Umatilla		N
				15.76[8]	Wanapum Basalt	Priest Rapids Member		
						Basalt of Lolo	15.92[3]	R
						Basalt of Rosalia		R
						Roza Member	15.92[4], 16.10[5]	T,R
						Shumaker Creek Member		N
						Frenchman Springs Member		
						Basalt of Sentinel Gap		N
						Basalt of Sand Hollow		N
						Basalt of Silver Falls	15.99[4]	N,E
						Basalt of Ginkgo	16.12[3]	E
						Basalt of Palouse Falls	16.12[3]	E
						Lookingglass Member		N
						Eckler Mountain Member		
						Basalt of Dodge	16.13[4]	N
						Basalt of Robinette Mountain		N
						Vantage Member of the Ellensburg Fm.	16.11[3], 16.13[4]	
	Lower			16.22[8]	Grande Ronde Basalt	**Sentinel Bluffs Member**	16.13[4], 16.15[5]	N_2
						Winter Water Member	16.22[3]	
				Picture Gorge Basalt	Prineville Basalt	Field Springs Member		
						Indian Ridge Member		
						Ortley member		
						Armstrong Canyon member		
						Buttermilk Canyon member		
						Slack Canyon Member	16.39[5]	
						Meyer Ridge Member	16.26[3]	R_2
						Grouse Creek member	16.27[4] 16.43[3]	
						Wapshilla Ridge Member	16.33[3]	
						Mt. Horrible member		
						Cold Spring Ridge Member	16.45[5]	N_1
						Hoskin Gulch Member	16.41[3]	
						China Creek Member	16.43[4]	
						Frye Point member		
						Downey Gulch Member	16.51[3]	?
						Brady Gulch member		
						Kendrick Grade member	16.47[3]	R_1
						Center Creek member		
						Skeleton Creek member		
						Rogersburg member		
						Teepee Butte Member		
						Birch Creek member		
						Buckhorn Springs Member	16.57[3,4], 16.58[3]	
					Imnaha Basalt		16.60[6], 16.57[4]	R_1 T N_0 R_0
				17.23[8]	Steens Basalt		16.54[8] 16.63[6], 16.64[4] ~16.75[8] 16.97[7]	

Figure 2. Chart showing stratigraphy and nomenclature for the CRBG. Modified from Reidel and others (2002) with updated stratigraphy from Reidel and others (2013a) and Reidel and Tolan (2013). Reported ages are from the following sources: [1]Barry and others (2013); [2]Ferns and others (2010); [3]Kasbohm and Schoene (2018) and Kasbohm and others (2023; U-Pb); [4]Kasbohm and others (2023; $^{40}Ar/^{39}Ar$); [5]Baksi (2022); [6]Mahood and Benson (2017); [7]Moore and others (2018); [8]Cahoon and others (2020, 2023). Bolded CRBG units either crop out at the surface or are present in the subsurface in the map area. Red lines show horizons of local erosional unconformities.

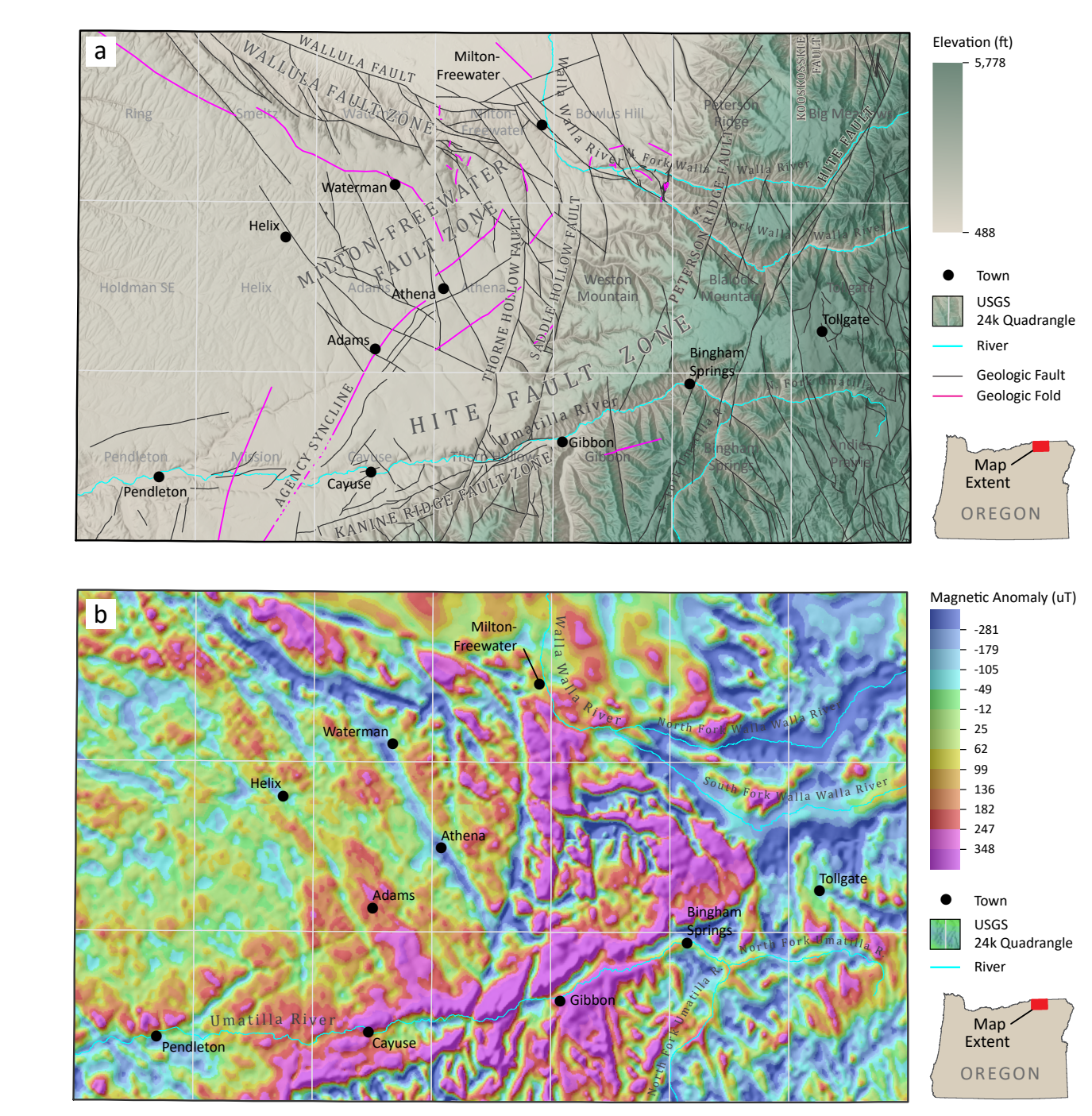

Figure 3. Structure maps of Adams and the surrounding area showing faults, folds, and high-resolution aeromagnetic data. (a) Mapped faults and folds drawn across a USGS 10-m DEM. (b) A total-field high-resolution aeromagnetic anomaly map of the area in (a) (Blakely and others, 2020a, b). The map in (b) shows a partially transparent classified color ramp of the magnetic data area overlain across a hillshade applied to the magnetic data. Mapped faults and folds shown are from this publication, McClaughry and Azzopardi (2023), Madin and others (2023), Darin and others (2025), and Guerrero and others (in press).

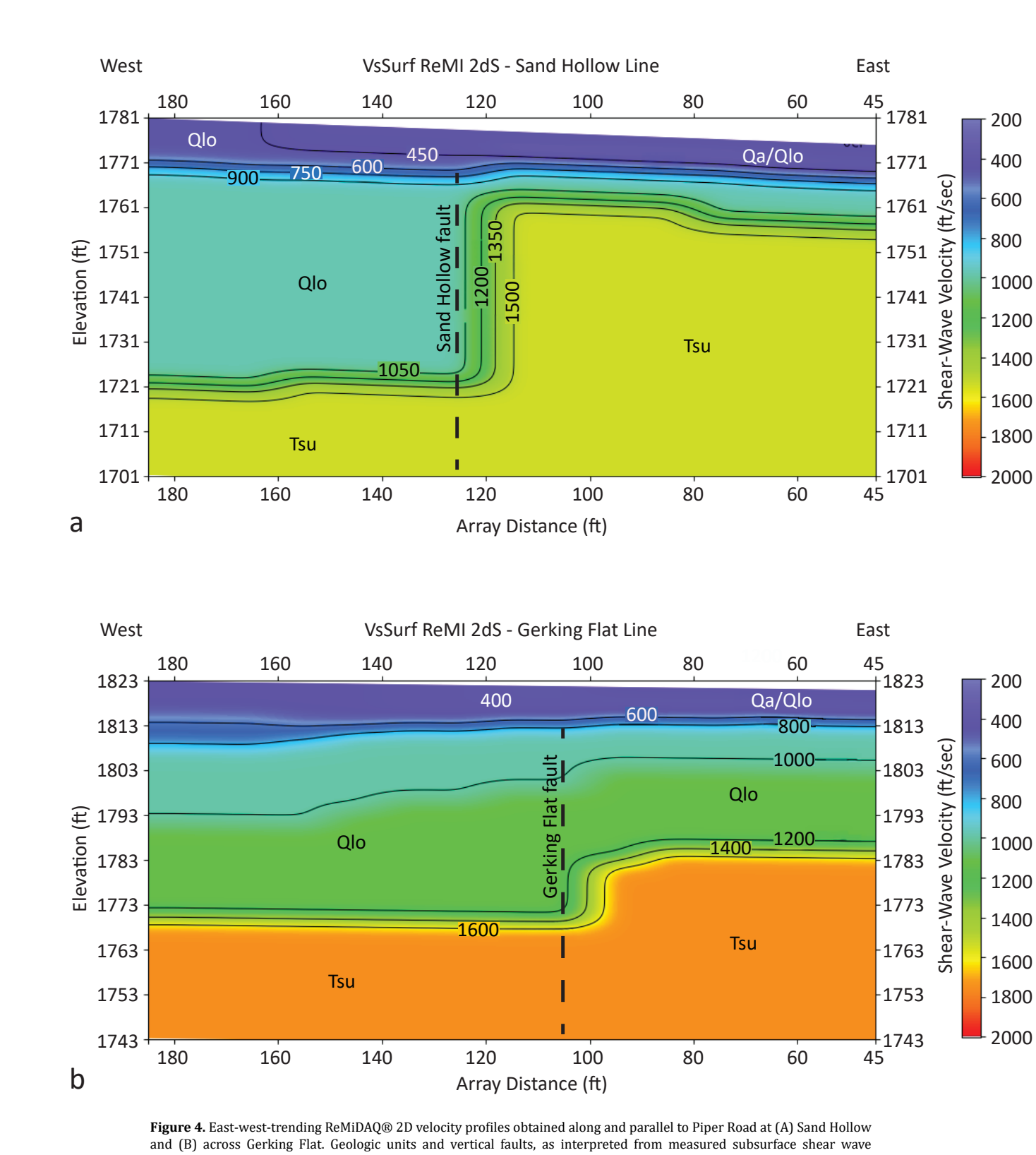

Figure 4. East-west-trending ReMiDAQ® 2D velocity profiles obtained along and parallel to Piper Road at (A) Sand Hollow and (B) across Gerking Flat. Geologic units and vertical faults, as interpreted from measured subsurface shear wave velocities, are labeled on the profiles. Green lines in figure 5, show the location of measured profiles in the Adams area.

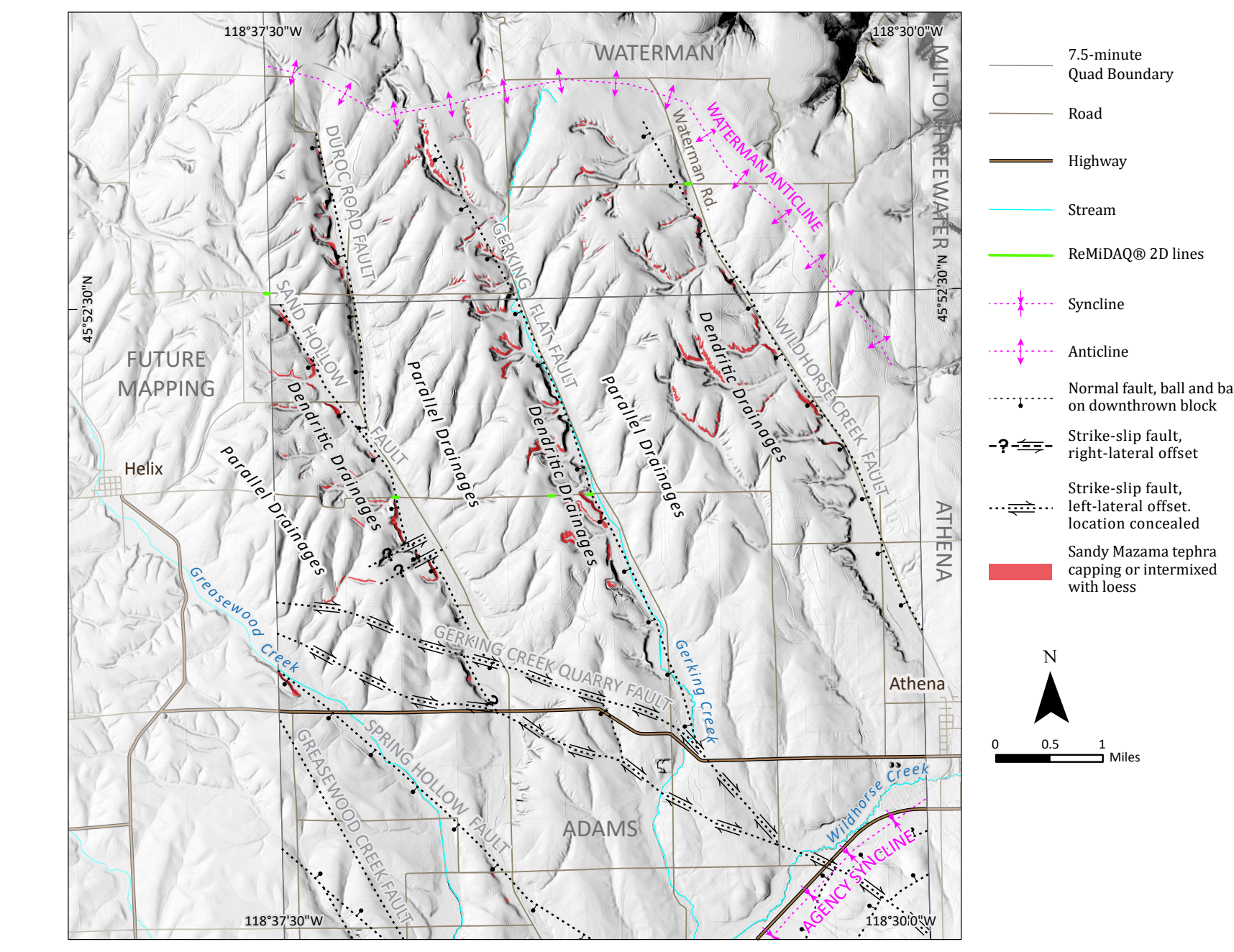

Figure 5. Landscape map illustrating the interrelations between underlying geologic structure and the distribution of parallel and dendritic drainage patterns developed on **Qlo** in the Adams and Waterman 7.5′ quadrangles. Faults, folds, and the overlay of Mazama tephra are from this publication and Guerrero and others (in press). The base map is a bare-earth 1-m lidar-derived DEM hillshade.

EXPLANATION OF MAP UNITS

UPPER CENOZOIC SURFICIAL DEPOSITS

Qf **modern fill and construction material (upper Holocene)**—Uncompacted to engineered and reinforced artificial or constructed deposits of poorly sorted and crudely layered mixed gravel, sand, clay, and other engineered fill (Plate 1). Areas mapped as **Qf** are generally associated with road embankments, dams and levees, culvert fills, and mined land (Plate 1). Older fills are likely uncompacted versus newer fills, which are likely engineered and reinforced using geotextiles or retaining structures. The thickness of fill deposits is as much as 30 m. **Qf** is assigned as late Holocene, ranging in age from the late 1800s to recent times.

Qls **landslide deposits (upper Holocene)**—Unconsolidated sand and silt and more coherent slump blocks deposited at the base of steep **Qlo** slopes in Sand Hollow (Plate 1). **Qls** is assigned a Holocene age as **Qlo** deposits forming head scarps contain ash and lapilli derived from the ~7700 cal. yr B.P. Plinian eruption of Mount Mazama (Bacon, 1983; Stuiver and others, 1998; Zdanowicz and others, 1999; Bacon and Lanphere, 2006; Bacon, 2008; Egan and others, 2015; Bacon and Wright, 2017).

Qa **alluvium (Holocene and Upper Pleistocene)**—Unconsolidated massive to variably stratified and cross-stratified gravel, sand, silt, and clay mapped in and adjacent to stream channels and on associated floodplains (Plate 1). Thickness of unit **Qa** is 1 to 6 m; bedrock units are locally exposed at the bases of stream channels within areas mapped as unit **Qa**. **Qa** is assigned a Late Pleistocene to Holocene age; the unit includes terraces hosting ash and lapilli derived from the ~7700 cal. yr B.P. Plinian eruption of Mount Mazama (Bacon, 1983; Stuiver and others, 1998; Zdanowicz and others, 1999; Bacon and Lanphere, 2006; Bacon, 2008; Egan and others, 2015; Bacon and Wright, 2017). Areas mapped as **Qa** may contain human-made debris or artifacts as well as other deposits modified by humans such as excavations, roadways, and gravel pits.

Qaf **fan deposits (Holocene and Upper Pleistocene)**—Unconsolidated, poorly sorted, poorly graded deposits of gravel, sand, silt, and clay in fan-shaped accumulations at the mouths of small and steep drainages (Plate 1). The local thickness of **Qaf** is variable but is commonly <15 m. **Qaf** includes fan deposits of Late Pleistocene and Holocene age.

Qlo **loess (Holocene to lower Pleistocene)**—Chiefly pale yellowish brown (10YR 6/2), micaceous, quartzo-feldspathic very fine sand-bearing, clay-silt mantling the CRBG (Plate 1). **Qlo** typically forms a massive, featureless deposit that has been pedogenically altered and contains bioturbated calcium carbonate- and clay-enriched paleosols with mm- to cm-scale beds, laminations, and lenses of primary and reworked tephra. **Qlo** has been extensively modified during the past century by dry-land agricultural cultivation; where **Qlo** is thin or has been subject to deep tilling, it may be mixed with weathered gravel-sized basalt clasts. **Qlo** is best exposed along roads, decommissioned railroad rights-of-way, and on poorly vegetated steep slopes that may reveal stacked sets of loessial paleosols and loess deposits whose cross-sectional geometry roughly parallels the modern landscape. **Qlo** is mapped here based on field observations, soils maps (Johnson and Makinson, 1988), geologic maps (Swanson and others, 1981; Madin and Geitgey; 2007), and interpretation of 1-m lidar DEMs and the 2020 NAIP orthophoto of Umatilla County (Plate 1). Most exposed contacts occur along human-modified boundaries between **Qlo** and older CRBG units.

Thickness of **Qlo** in the Adams 7.5′ quadrangle is variable over the map area as discerned from well logs and ReMiDAQ® 2D velocity profiles, (Figure 4; Plate 1). The thickest accumulations of **Qlo** are found along the eastern edges of the ~N20°W-trending ridges separated by four parallel alluvial valleys in the northern half of the quadrangle (Plate 1). The thickness of **Qlo** is as much as 25 m west of Greasewood Creek at the city of Helix (outside the map area, 5 km west-northwest of Sand Hollow, e.g., UMAT 5351), 35 m west of Sand Hollow (e.g., ReMiDAQ® 2D velocity profile; UMAT 3039), 35 m west of Gerking Flat (e.g., ReMiDAQ® 2D velocity profile), and 30 m west of Waterman Road (e.g., UMAT 3039). **Qlo** is as much as 21 m thick across hillcrests west of Greasewood Creek (e.g., UMAT 51779, UMAT 3047; Figure 4; Plate 1). Roadcuts on western slopes between Gerking Flat and Sand Hollow locally reveal up to 6–10 m of **Qlo** in vertical section (e.g., Piper Road, 0.5 km east of Sand Hollow Road; Sand Hollow Road, 0.5 km west of the intersection with Duroc Road; Plate 1). **Qlo** thins to the east and southeast to 14 m along Waterman Road in the eastern part of the map area (e.g., UMAT 3042), 7 m at the city of Adams (e.g., UMAT 5331), 3 m southeast of Wildhorse Creek (UMAT 1428), and 5 m at the city of Athena (e.g., UMAT 57710; McClaughry and Azzopardi, 2023; Plate 1). Loess deposits <1 m thick are not mapped.

Qlo in the Adams 7.5′ quadrangle is part of the Palouse, a loess-dominated landscape that mantles >50,000 km^2 of the Columbia Plateau in southeastern Washington, northwestern Idaho, and northeastern Oregon (Figure 1). The uppermost Palouse loess deposits have been subdivided informally into the L1, L2, L3 (youngest to oldest) loess sequences (McDonald and others, 2012) dating back ~70,000 years; normal-reversed-normal polarity signatures indicate underlying loess deposits date back 1–2 million years (Patton and Baker, 1978; Waitt, 1985; McDonald and Busacca, 1988; Busacca, 1989; Bjornstad and others, 2001; Pluhar and others, 2006; Baker, 2009). Morphologically, the Palouse is subdivided into a northeastern part characterized by a dendritically drained, rolling landscape of very fine sand-bearing, clay-silt loess with 5–20 m of relief and a southwestern part characterized by subparallel to parallel, 10–20 m high, 1–5 km long, N30°E-trending linear ridges bordered by similarly aligned valleys (Lewis, 1960). The southwestern Palouse extends from near Pendleton, Oregon, to the Palouse River west of Colfax, Washington (~20 km northwest of Pullman); the northeastern Palouse extends from the Palouse River across eastern Washington to northwestern Idaho. **Qlo** particle-size data from a detailed SW-NE traverse across the Palouse (Lewis, 1960) revealed a downwind (southwest-to-northeast) decrease in median particle size from coarse silt in the southwestern Palouse to medium silt in the northeastern Palouse. Notably, Lewis (1960) did not address the complex morphology of loess deposits east of the prominent linear loess ridges he used to characterize the southwestern Palouse. As described in the 'interrelations between structure and geomorphology' subsection, the morphologies of the easternmost southwestern Palouse **Qlo** include topographically subdued, though much less numerous, N20°E–N30°E-trending linear ridges as well as a fault-influenced and dendritically drained loess landscape.

Qlo in the Adams 7.5′ quadrangle is assigned a Pleistocene and Holocene age based on its chronostratigraphic correlation with the northern Palouse loess in Washington (McDonald and others, 2012; Figure 1). The thickest and most laterally continuous loess contains intercalated deposits of ash and lapilli (tephra), including an ~4 cm thick, conspicuously white (N9) to pinkish gray (5YR 8/1), massive to planar-stratified deposit exposed in the upper part of a 10-m-high vertical roadcut (6.5 m above road level) 0.5 km west of the intersection of Sand Hollow Road and Duroc Road (Figure 6a, Plate 1). Electron microprobe analyses of 17 glass shards from a sample of this tephra indicate a statistical correlation with tephra layer 5-42A recovered from a Walker Lake, Nevada sediment core (Herrero-Bervera and others, 1994; map no. G45; Table 2). Although no direct age date exists for tephra layer 5-42A, Herrero-Bervera and others (1994) constrained an age for the tephra in Nevada between ~171 and ~130 ka.

Significant accumulations of tephra are also recognized and mapped near the upper part of **Qlo**, where the unit is notably dissected by a set of dendritic drainages on the east side of three parallel NNW-trending ridges north of the Greasewood Creek quarry fault in the Adams 7.5′ quadrangle (Plate 1). Plate 1 illustrates the distribution of these tephra deposits as a stippled overlay of areas where concentrations of sandy Mazama tephra cap or are intermixed with **Qlo**. In the field, areas of Mazama tephra are often revealed in the active excavations of badgers who have burrowed into steep, east-dipping steep **Qlo** slopes (Figure 6b). The most distinctive exposures of Mazama tephra in the Adams 7.5′ quadrangle are found in east-facing unvegetated eolian sand blowouts exposed along a ~10 m high loess ridge along the west side of Sand Hollow Road, south of its intersection with Piper Road and in exposures in the headwall cuts of the Humbert Landfill west of Gerking Flat (Plate 1, Figure 6c-f). Borehole drilling in Sand Hollow indicates tephra-rich blowouts there are laterally discontinuous, with very light gray (N8) tephra concentrated in 3.1 to >5.1 m thick lens-shaped deposits. Planar-stratified very light gray (N8) tephra deposits exposed in the headwall of Humbert Landfill are ~1 to 2 m thick, mantling the east-facing slope (leeward side) and infilling an erosional unconformity on older Pleistocene loess **Qlo** (Figure 6e—g). Tephra is overlain by intensely burrowed Holocene loess (Figure 6e—g). Electron microprobe analyses of 103 glass shards from 4 samples collected at the Sand Hollow and Humbert Landfill localities have a statistical correlation with the ~7700 cal. yr B.P. climactic Plinian eruption of Mount Mazama (Bacon, 1983; Stuiver and others, 1998; Zdanowicz and others, 1999; Bacon and Lanphere, 2006; Bacon, 2008; Egan and others, 2015; Bacon and Wright, 2017; Table 2; map nos. G37, G38, G39, G43). Similar accumulations of tephra, chemically matched to Mount Mazama, have also been found in the southern parts of the Waterman and Smeltz 7.5′ quadrangles on the north and northwest (Guerrero and others, in press).

mt Stippled overlay pattern depicts areas where concentrations of sandy Mazama tephra (Holocene) cap or are intermixed with loess.

Unconformity

UPPER CENOZOIC VOLCANIC AND SEDIMENTARY ROCKS

COLUMBIA RIVER BASALT GROUP

The Columbia River Basalt Group (CRBG) is an extensive succession of tholeiitic basalt and basaltic andesite lava flows covering more than 210,000 km^2 in parts of Washington, Oregon, Idaho, and Nevada (Reidel and others, 2013a; Figures 1, 2). In the Adams 7.5′ quadrangle, CRBG lava flows largely underlie an extensive cover of early Pleistocene to Holocene loess (**Qlo**). Only the Umatilla Member (**Tsu**) of the Saddle Mountains Basalt and the uppermost part (**Twfsl**) of the Frenchman Springs Member of the Wanapum Basalt crop out in the map area. Older units of the Wanapum and Grande Ronde Basalt are only present in the subsurface (Figure 2, Plate 1, cross sections). These older units appear here only in cross-section based on detailed mapping in the surrounding Waterman, Milton-Freewater, Athena, Cayuse, and Mission 7.5′ quadrangles and geochemical identification in water wells in the Adams, Athena, and Helix 7.5′ quadrangles (Ferns, 2006; Ferns and Ely, 2006; McClaughry and Azzopardi, 2023; Madin and others, 2023; Guerrero and others, in press; Figure 2; Plate 1, cross section A—A′;). Aggregate thickness of the CRBG in the Adams 7.5′ quadrangle exceeds 525 m.

Saddle Mountains Basalt

The Saddle Mountains Basalt erupted between ~14 and 6 Ma and represents the longest eruptive period of all CRBG formations (Figure 2). Regionally, Saddle Mountains lava flows are confined by paleotopography and form thick, channelized, or dammed lava flows characterized by well-developed columnar jointing. The Saddle Mountains Basalt is represented by the Umatilla Member in the map area:

Umatilla Member

Tsu **Umatilla Member (middle Miocene)**—High-titanium and iron-rich basaltic trachyandesite to trachyandesite lava flows (SiO_2 = 53.28–56.24 weight percent; TiO_2 = 2.61–3.16 weight percent; n = 13 analyses, 2 outside map area) characterized by high potassium (K_2O = 2.43–2.88 weight percent), phosphorus (P_2O_5 = 0.73–1.06 weight percent), and barium (Ba = 2695–3620 ppm; Figures 2, 7; Table 1). **Tsu** is mapped extensively beneath **Qlo** in the Adams 7.5′ quadrangle, with the exception of the area southwest of the Adams fault (Plate 1, cross section B—B′). The Umatilla Member consists of two chemically distinctive lava flows that are both present in the map area (Laval, 1956; Reidel and others, 2013a; Figures 2, 7). The older Basalt of Umatilla has titanium contents >2.9 weight percent TiO_2, phosphorous contents <0.9 weight percent P_2O_5, and barium contents <3000 ppm; the younger Basalt of Sillusi has titanium contents <2.9 weight percent TiO_2, phosphorous contents >0.9 weight percent P_2O_5, and barium contents >3000 ppm (Nersinger, 2021; McClaughry and Azzopardi, 2023; Madin and others, 2023; Figures 2, 7; Table 1). Based on well logs, the lava flows are underlain in places by tuffaceous sedimentary rocks (e.g., UMAT 3039; Mabton Member of the Ellensburg Formation). The thickness of **Tsu** is 34 m in water well UMAT 5331 at Adams, 38 m in water well UMAT 5351 at Helix (outside the northwest corner of the quadrangle), and 35 m in water well UMAT 57710 at Athena (outside the east-central boundary of the quadrangle; Figure 5, Plate 1, cross sections). Typical hand samples are medium gray (N5) to medium bluish gray (5B 5/1) and aphyric to very sparsely porphyritic with rare plagioclase and olivine phenocrysts <2 millimeters (mm) distributed in a fine- to very fine-grained holocrystalline groundmass. Both the Basalt of Sillusi and the Basalt of Umatilla have normal magnetic polarity (Figure 2). **Tsu** is assigned a middle Miocene age based on stratigraphic position and isotopic ages. The U.S. Energy Research and Development Administration reported a K-Ar age of 14.57 Ma for the Umatilla Member (1976; recalculated by Barry and others, 2013) while Ferns and others (2010) obtained an $^{40}Ar/^{36}Ar–^{40}Ar/^{39}Ar$ isochron age of 13.64 + 0.17 Ma in the upper Grande Ronde River basin (Figure 2).

Disconformity—Mabton Member of the Ellensburg Formation

Wanapum Basalt

The Wanapum Basalt in the Adams 7.5′ quadrangle consists of lava flows assigned to the Frenchman Springs Member (Figure 2). In the map area, Wanapum Basalt differs from the older Grande Ronde Basalt by the presence of widely scattered to conspicuous large plagioclase phenocrysts and markedly higher titanium contents (Figure 7, Table 1). U-Pb ages from silicic tuff interbeds between lava flows on the Columbia Plateau constrained the eruption of the Frenchman Springs Member between 16.1 and 15.9 Ma (Kasbohm and Schoene, 2018; Kasbohm and others, 2023). Additional $^{40}Ar/^{39}Ar$ dating by Baksi (2022) further refined the eruption ages of the entirety of the Frenchman Springs Member to ~16.1 Ma. The Wanapum Basalt is subdivided in the map area into the following units:

Frenchman Springs Member

Basalt of Sentinel Gap (lower Miocene)—Flow-on-flow sequence of high-titanium and iron-rich basalt lava flows (SiO_2 = 50.89–53.71 weight percent; TiO_2 = 3.00–3.30 weight percent; P_2O_5 = 0.58–0.69 weight percent; n = 18 analyses, 6 outside map area) mapped in the western and southern parts of the Adams 7.5′ quadrangle (Figures 2, 7; Table 1; Plate 1, cross sections). The stratigraphically lowest geologic unit cropping out in the Adams 7.5′ quadrangle is the low-phosphorous lava flows (**Twfsl**) that form the upper part of the Basalt of Sentinel Gap (Plate 1, cross sections). Dikes correlated with the Basalt of Sentinel Gap (**Twfsl**, **Twfsh**) have been mapped between the Thorn Hollow and Saddle Hollow faults in the adjacent Athena 7.5′ quadrangle (McClaughry and Azzopardi, 2023). The Basalt of Sentinel Gap (**Twfsl**, **Twfsh**) is distinguished from the underlying Basalt of Sand Hollow (**Twfh**) by its relatively higher amounts of titanium (avg TiO_2 = 3.07 weight percent) and phosphorus (avg P_2O_5 = 0.60 weight percent) and lesser amounts of chromium (avg Cr = 17 ppm; Figures 2, 7; Table 1). Thickness of the Basalt of Sentinel Gap (**Twfsl**, **Twfsh**) is as much as 165 m in the southern part of the map area and 125 m across the northern part of the map area (Plate 1, cross sections). Typical hand samples are medium dark gray (N4) to dark gray (N2) and aphyric to very sparsely porphyritic with <1 percent volume clear to pale yellowish orange (10YR 8/6) plagioclase microphenocrysts and phenocrysts ≤7 mm and <2 percent volume grayish black (N2) clinopyroxene microphenocrysts, enclosed within a fine-grained holocrystalline to hypocrystalline groundmass of plagioclase, intergranular clinopyroxene, iron-titanium oxides, and intersertal glass. The Basalt of Sentinel Gap (**Twfsl**, **Twfsh**) has normal magnetic polarity and an age between 16.1 and 15.9 Ma (Figure 2). Subdivided in the map area into the following units:

Twfsl **Basalt of Sentinel Gap, low-phosphorus lava flows (lower Miocene)**—Flow-on-flow sequence of high-titanium and lower-phosphorus basalt lava flows (SiO_2 = 50.89–53.71 weight percent; TiO_2 = 3.03–3.30 weight percent; P_2O_5 = 0.58–0.64 weight percent; n = 15 analyses, 5 outside map area) mapped in the western and southern parts of the Adams 7.5′ quadrangle (Figures 2, 7; Table 1, Plate 1, cross sections). **Twfsl** is additionally recognized from cuttings retrieved from wells UMAT 5331 at Adams (see map nos. G08 to G11), UMAT 5351 at Helix (outside map area), and UMAT 57710 at Athena (outside map area; McClaughry and Azzopardi, 2023). Thickness of **Twfsl** is 80 m in water well UMAT 5331 at Adams, 61 m in water well UMAT 5351 at Helix, and 74 m in water well UMAT 57710 at Athena (Figure 5, Plate 1, cross sections).

Twfsh **Basalt of Sentinel Gap, high-phosphorus lava flows (lower Miocene) (cross section only)**—Flow-on-flow sequence of high-titanium and higher-phosphorus basalt lava flows (SiO_2 = 51.74–53.53 weight percent; TiO_2 = 3.0–3.12 weight percent; P_2O_5 = 0.65–0.69 weight percent; n = 3 analyses, 1 outside map area) lying beneath **Twfsl** and above **Twfh** in the Adams 7.5′ quadrangle (Figures 2, 7; Table 1; Plate 1, cross sections). Recognized in the area only from cuttings retrieved from well UMAT 5331 at Adams (see map nos. G12 and G13), UMAT 5351 at Helix (outside map area), and UMAT 57710 at Athena (outside map area; McClaughry and Azzopardi, 2023). Thickness of **Twfsh** is 85 m in water well UMAT 5331 at Adams, 45 m in water well UMAT 5351 at Helix, and 48 m in water well UMAT 57710 at Athena (Figure 5, Plate 1, cross sections).

Twfh **Basalt of Sand Hollow (lower Miocene) (cross section only)**—Flow-on-flow sequence of high-titanium basalt lava flows (SiO_2 = 50.98–53.3 weight percent; TiO_2 = 2.65–3.16 weight percent; P_2O_5 = 0.53–0.6 weight percent; n = 9 analyses, 6 outside map area) lying beneath **Twfsh** and above **Tgsmu** in the Adams 7.5′ quadrangle (Figures 2, 7; Table 1, Plate 1, cross sections). **Twfh** appears only in cross-section in the Adams 7.5′ quadrangle and is recognized in the map area only from cuttings retrieved from water wells UMAT 5331 at Adams (see map nos. G14 to G16), UMAT 5351 at Helix (outside map area), and UMAT 57710 at Athena (outside map area; McClaughry and Azzopardi, 2023). **Twfh** is distinguished from overlying **Twfsh** by higher amounts of chromium (avg Cr = 49 ppm), lower titanium (avg TiO_2 = 2.98 weight percent) and phosphorus (avg P_2O_5 = 0.57 weight percent), and higher magnesium (avg MgO = 4.16 weight percent) than other Frenchman Springs units (Figures 2, 7; Table 1). Thickness of **Twfh** is 55 m in water well UMAT 5331 at Adams, 115 m in water well UMAT 5351 at Helix, and 79 m in water well UMAT 57710 at Athena (Figure 5, Plate 1, cross sections). **Twfh** has normal magnetic polarity and an age between 16.1 and 15.9 Ma (Figure 2).

Disconformity

Grande Ronde Basalt

The Grande Ronde Basalt is the thickest, most voluminous formation of the CRBG (Reidel and Tolan, 2013). The formation spans at least four paleomagnetic zones and has been stratigraphically subdivided into four normal and reversed polarity magnetostratigraphic units (R1, N1, R2, N2) by Swanson and others (1979; Figure 2). No Grande Ronde lava flows crop out at the surface in the Adams 7.5′ quadrangle, but several members have been interpreted to be present in the subsurface, based on geochemical analyses of well cuttings retrieved from water wells in the cities of Helix, Adams, and Athena. Grande Ronde lava flows identified through geochemistry beneath the map area, include the Sentinel Bluffs (**Tgsmu**, **Tgsmc**), Winter Water (**Tgww**), and Grouse Creek (**Tgcc**) members (Figure 2, Plate 1, cross sections). Mapping to the east suggests the Indian Ridge (**Tgir**), Ortley (**Tgo**), and Buttermilk Canyon (**Tgbc**) members are likely also present at depth (McClaughry and Azzopardi, 2023; Madin and others, 2023). Grand Ronde lava flows are generally monotonously fine-grained, aphyric, and texturally non-distinctive tholeiitic basalts and basaltic andesites with relatively homogeneous chemical compositions (Table 1). The Grande Ronde Basalt differs from the overlying Wanapum Basalt by the local presence of the intervening Vantage Member of the Ellensburg Formation, the conspicuous absence of large plagioclase phenocrysts and glomerocrysts, and significantly lesser titanium contents (Swanson and others, 1979; Hooper, 2000; Tolan and others, 2009; Figure 7, Table 1).

Normal-polarity (N2) magnetostratigraphic:

The N2 magnetostratigraphic unit is the youngest Grande Ronde Basalt magnetostratigraphic unit, covering ~114,500 km^2 with an estimated volume of 35,300 cubic kilometers (km^3; Reidel and Tolan, 2013; Figure 2). Ages of N2 Grande Ronde units are bracketed by U-Pb dates of 16.134 ± 0.037 Ma from the white mud at the base of the overlying Vantage Member and 16.260 ± 0.036 Ma from the red clay (bole) between the underlying Meyer Ridge and Wapshilla Ridge members of the R2 magnetostratigraphic unit (Kasbohm and others, 2023; Figure 2). Subdivided in the map area into the following units:

Sentinel Bluffs Member

Sentinel Bluffs Member (lower Miocene) (cross section only)—Flow-on-flow sequence of high-magnesium basaltic andesite lava flows (SiO_2 = 53.10–55.12 weight percent; TiO_2 = 1.75–2.17 weight percent; MgO = 4.12–5.26 weight percent; n = 15 analyses, 5 outside map area) lying beneath the Frenchman Springs Member (**Twfh**) and above the Winter Water Member (**Tgww**) in the Adams 7.5′ quadrangle (Figures 2, 7; Table 1, Plate 1, cross sections). The Sentinel Bluffs Member (**Tgsmu**, **Tgsmc**) differs from other members of the Grande Ronde Basalt in the map area on the basis of lesser amounts of silica (avg SiO_2 = 54.29 weight percent) and higher magnesium contents (avg MgO = 4.7 weight percent; Figures 2, 7; Table 1). Thickness of the Sentinel Bluffs Member (**Tgsmu**, **Tgsmc**) is as much as 105 m in cross section (Plate 1, cross sections). The Sentinel Bluffs Member (**Tgsmu**, **Tgsmc**) has normal magnetic polarity and an age of between 16.2 and 16.1 Ma (Figure 2). Subdivided in the map area into the following units:

Tgsmu **Basalt of Museum (lower Miocene) (cross section only)**—Basaltic andesite lava flows (SiO_2 = 54.39–55.12 weight percent; TiO_2 =1.75–1.86 weight percent; MgO = 4.61–4.85 weight percent; n = 3 analyses) mapped at the top of the Sentinel Bluffs Member in the Adams 7.5′ quadrangle (Figures 2, 7; Table 1; Plate 1, cross sections). **Tgsmu** only appears in cross-section in the Adams 7.5′ quadrangle. Recognized in the area only from cuttings retrieved from well UMAT 5331 at Adams (see map nos. G17 to G19), UMAT 5351 at Helix (outside map area), and UMAT 57710 at Athena (outside map area; McClaughry and Azzopardi, 2023). Distinguished from underlying unit **Tgsmc** based on lesser contents of titanium (avg TiO_2 = 1.79 weight percent; Figures 2, 7; Table 1). Thickness of **Tgsmu** is 35 m in water well UMAT 5331 at Adams, 61 m in water well UMAT 5351 at Helix, and 63 m in water well UMAT 57710 at Athena (Figure 5, Plate 1, cross sections). Kasbohm and others (2023) reported an $^{40}Ar/^{39}Ar$ groundmass age of 16.135 ± 0.04 Ma. Baksi (2022) reported a similar $^{40}Ar/^{39}Ar$ plateau age of 16.15 ± 0.07 Ma (Figure 2).

Tgsmc **Basalt of McCoy Canyon (lower Miocene) (cross section only)**—Basaltic andesite lava flows (SiO_2 = 53.1–55.05 weight percent; TiO_2 =1.87–2.17 weight percent; MgO = 4.12–5.26 weight percent; n = 12 analyses, 5 outside map area) mapped below **Tgsmu** and above **Tgww** in the Adams 7.5′ quadrangle (Figures 2, 7; Table 1, Plate 1, cross sections). **Tgsmc** appears only in cross-section in the Adams 7.5′ quadrangle. Recognized in the area only from cuttings retrieved from well UMAT 5331 at Adams (see map nos. G20 to G26), UMAT 5351 at Helix (outside map area), and UMAT 57710 at Athena (outside map area; McClaughry and Azzopardi, 2023). Distinguished from overlying unit **Tgsmu** based on higher contents of titanium (avg TiO_2 = 2.02 weight percent) and from underlying **Tgww** by higher amounts of magnesium (avg MgO = 4.67 weight percent; Figures 2, 7; Table 1). Thickness of **Tgsmc** is 69 m in water well UMAT 5331 at Adams, 30 m in water well UMAT 5351 at Helix, and 41 m in water well UMAT 57710 at Athena (Figure 5; Plate 1, cross sections).

Winter Water Member

Tgww **Winter Water Member (lower Miocene) (cross section only)**—Basaltic andesite lava flows (SiO_2 = 55.05–56.61 weight percent; TiO_2 = 2.17–2.3 weight percent; MgO = 2.78–3.79 weight percent; n = 5 analyses, 1 outside map area) lying below **Tgsmc** and above **Tgir** in the Adams 7.5′ quadrangle (Figures 2, 7; Table 1, Plate 1, cross sections). **Tgww** appears only in cross-section in the Adams 7.5′ quadrangle. The unit is recognized in the area only from cuttings retrieved from well UMAT 5331 at Adams (see map nos. G27 to G30), UMAT 5351 at Helix (outside map area), and UMAT 57710 at Athena (outside map area; McClaughry and Azzopardi, 2023). **Tgww** is distinguished from overlying units **Tgsmu** and **Tgsmc** by lesser amounts of magnesium (avg MgO = 3.34 weight percent; Figures 2, 7; Table 1). Thickness of **Tgww** is at least 53 m in water well UMAT 5331 at Adams and 55 m in water well UMAT 57710 at Athena (Figure 5, Plate 1, cross sections). The unit was sampled at a 375 m depth interval in water well UMAT 5351 at Helix (outside the northwest corner of the quadrangle) but the total thickness of the unit is not known. **Tgww** has normal magnetic polarity and an age between 16.2 and 16.1 Ma (Figure 2).

Indian Ridge Member

Tgir **Indian Ridge Member (lower Miocene) (cross section only)**—Basaltic andesite lava flows shown beneath **Tgww** and above **Tgo** in cross section in the Adams 7.5′ quadrangle. The unit is interpreted to be present in the subsurface based on nearby detailed mapping in the Milton-Freewater and Athena 7.5′ quadrangles to the northeast and east (McClaughry and Azzopardi, 2023; Madin and others, 2023; Plate 1, cross sections). **Tgir** has normal magnetic polarity and an age between 16.2 and 16.1 Ma (Figure 2).

Ortley member

Tgo **Ortley member (lower Miocene) (cross section only)**—Basaltic andesite lava flows shown beneath **Tgir** and above **Tgbc** appearing only in cross section in the Adams 7.5′ quadrangle. The unit is interpreted to be present in the subsurface based on nearby detailed mapping in the Milton-Freewater and Athena 7.5′ quadrangles to the northeast and east (McClaughry and Azzopardi, 2023; Madin and others, 2023; Plate 1, cross sections). **Tgo** has normal magnetic polarity and an age of 16.3-16.2 Ma (Figure 2).

Buttermilk Canyon member

Tgbc **Buttermilk Canyon member (lower Miocene) (cross section only)**—Basaltic andesite lava flows shown beneath **Tgo** and above **Tggc** in cross section in the Adams 7.5′ quadrangle. The unit is interpreted to be present in the subsurface based on nearby detailed mapping and water well interpretation in the Milton-Freewater and Athena 7.5′ quadrangles to the northeast and east (McClaughry and Azzopardi, 2023; Madin and others, 2023; Plate 1, cross sections). **Tgbc** is present in water well UMAT 57710 at Athena, where it is 41 m thick (McClaughry and Azzopardi, 2023). **Tgbc** has normal magnetic polarity and an age between 16.3 and 16.2 Ma (Figure 2).

Reversed-polarity (R2) magnetostratigraphic unit and Normal-polarity (N1) magnetostratigraphic unit

The R2 magnetostratigraphic unit is the most aerially extensive and voluminous of the four Grande Ronde Basalt magnetostratigraphic units, covering ~117,730 km^2 with an estimated volume of 56,000 km^3 (Reidel and Tolan, 2013; Figure 2). Kasbohm and others (2023) reported U-Pb ages for the R2 magnetostratigraphic unit of 16.260 ± 0.036 Ma and 16.327 ± 0.040 Ma (Figure 2). These workers obtained an $^{40}Ar/^{39}Ar$ plateau age of 16.269 ± 0.036 Ma for the Wapshilla Ridge Member of the R2 magnetostratigraphic unit. Baksi (2022) stated $^{40}Ar/^{39}Ar$ plateau ages of 16.43 ± 0.04 Ma and 16.44 ± 0.06 Ma for the middle and lower parts of the R2 unit magnetostratigraphic unit and an $^{40}Ar/^{39}Ar$ plateau age of 16.43 ± 0.09 Ma for the uppermost part of the N1 magnetostratigraphic unit, placing the R2-N1 boundary in the Grande Ronde Basalt at ~16.45 Ma.

Grouse Creek member

Tggc **Grouse Creek member (lower Miocene) (cross section only)**—Basaltic andesite lava flows interpreted to be present beneath **Tgbc** in the Adams 7.5′ quadrangle (Plate 1, cross section A—A′). The presence of **Tggc** in the subsurface in the map area is recognized by a single analysis on a sample retrieved from a depth of 526 m in water well UMAT 5331 at Adams (see map no. G31, Table 1). The sample from the 526 m depth in UMAT 5331 is a basaltic andesite (SiO_2 = 55.66 weight percent; TiO_2 =1.74 weight percent; MgO = 4.27 weight percent; n = 1 analyses) comparable to the Grouse Creek member mapped east in the Bowlus Hill area by Madin and others (2023; avg TiO_2 = 1.77 weight percent, avg MgO = 4.46 weight percent; n = 6 analyses). This sample represents the stratigraphically lowest sample in the map area. The thickness of **Tggc** in the area is unknown, as water well UMAT 5331 did not penetrate the entire unit. Grande Ronde Basalt is likely to extend deeper in the map area but it is not sampled or penetrated by local wells (Plate 1, cross section A—A′). **Tggc** has reversed magnetic polarity and an age of ~16.3 Ma (Figure 2).

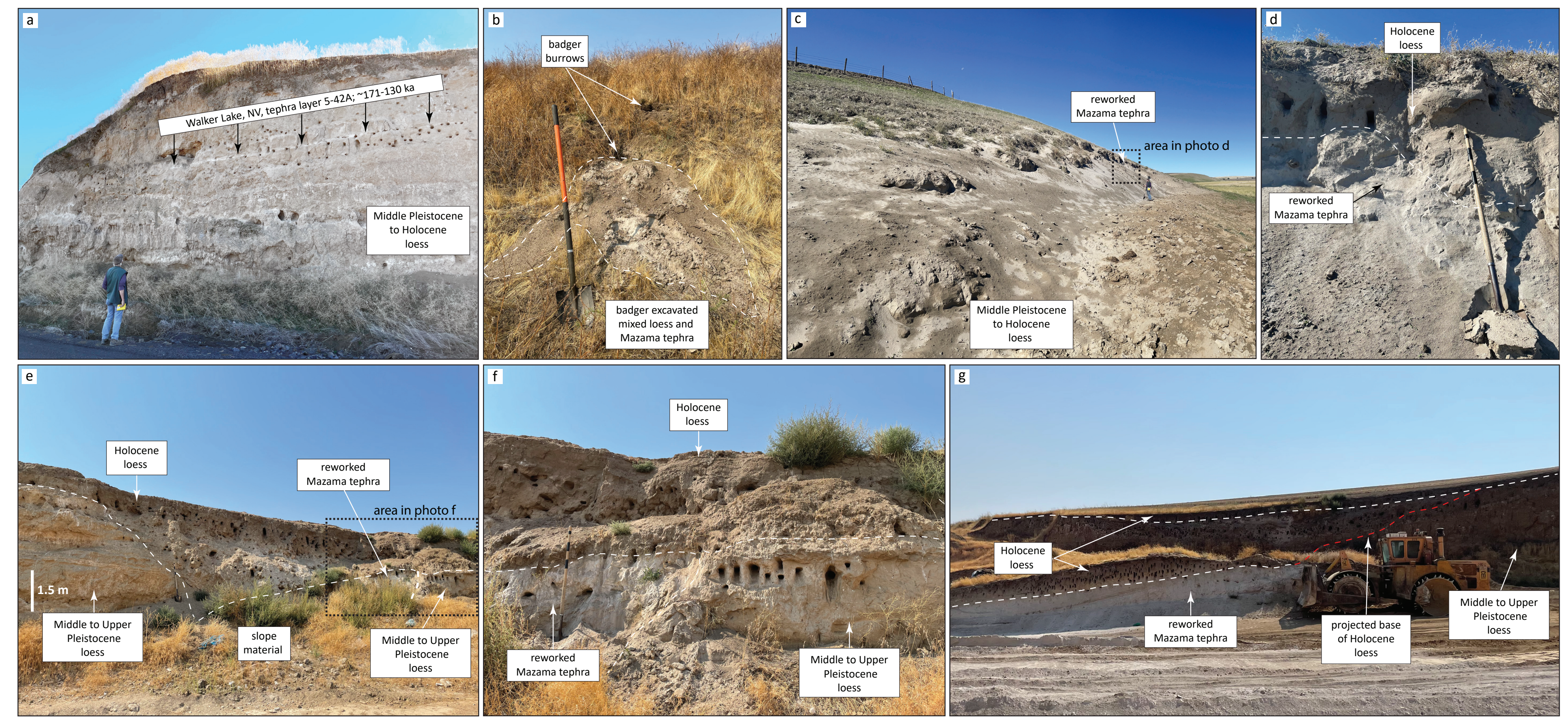
a
Walker Lake, NV, tephra layer 5-42A; ~171-130 ka
Middle Pleistocene to Holocene loess
b
badger burrows
badger excavated mixed loess and Mazama tephra
c
reworked Mazama tephra
area in photo d
Middle Pleistocene to Holocene loess
d
Holocene loess
reworked Mazama tephra
e
Holocene loess
reworked Mazama tephra
area in photo f
1.5 m
Middle to Upper Pleistocene loess
slope material
Middle to Upper Pleistocene loess
f
Holocene loess
reworked Mazama tephra
Middle to Upper Pleistocene loess
g
Holocene loess
reworked Mazama tephra
projected base of Holocene loess
Middle to Upper Pleistocene loess

Figure 6. Examples of loess (**Qlo**) interbedded with tephra in the Adams 7.5′ quadrangle. (a) A 10-m-high vertical roadcut of Middle Pleistocene to Holocene loess along Sand Hollow Road, 0.5 km west of the intersection with Duroc Road (45.861634, -118.615161). Roadcut includes a conspicuously white (N9) to pinkish gray (5YR 8/1) ~4-cm-thick planar bedded tephra (see black arrows) correlated to the ~171–130 ka 5-42A tephra collected from a Walker Lake, Nevada, sediment core. The view is to the south; the person for scale is 1.6 m tall. (b) East-facing slope of Holocene loess and reworked ~7700-calendar yr B.P. Mazama tephra revealed by badger-burrow excavations (45.84859, -118.56551). Excavations are outlined by a dashed white line. The view is to the west and the shovel for scale is 1.5 m tall. (c) Notable accumulations of loess and interstratified sand-rich Mazama tephra in unvegetated eolian sand blowouts in east-facing slopes along the west side of Sand Hollow, south of Piper Road (45.840682, -118.597514). The view is to the north toward a 1.6 m tall person for scale. The black square is the location of the inset photograph shown in (d). (d) Close-up view of the north end of the same outcrop as in (c). Pale yellowish brown (10YR 6/2) micaceous, quartzo-feldspathic very fine sand- and clay-silt–dominated Holocene loess here overlies a 1.5-m-thick bed of reworked Mazama tephra (45.84086, -118.59789). The white dashed line marks the contact between the subunits. The view is to the west; the shovel for scale is 1.5 m tall. (e) Erosional unconformity on top of Middle to Upper Pleistocene loess, infilled by reworked Mazama tephra and Holocene loess in the upper part of the Humbert Landfill (45.83621, -118.56117). The view is to the west; a vertical scale bar in the left of the photograph is 1.5 m tall. The black square shows the location of the inset photograph shown in (f). (f) Close-up view of the outcrop in (e) revealing the stratigraphic relations between Mazama tephra and dominantly Holocene loess overlying Middle to Upper Pleistocene loess. The view is to the west; the shovel for scale is 1.5 m. The white dashed lines mark the contacts between subunits in both (e) and (f). (g) A west-dipping stratigraphic section of reworked, planar-stratified Mazama tephra overlain by intensely burrowed Holocene loess in the Humbert Landfill (45.83569, -118.56043). The subunits are separated by dashed white lines; the red-dashed line projects this contact west to the landfill highwall. The view is looking south; the bulldozer for scale is ~4 m tall. Geographic locations for all photographs are given in WGS84 geographic coordinates.

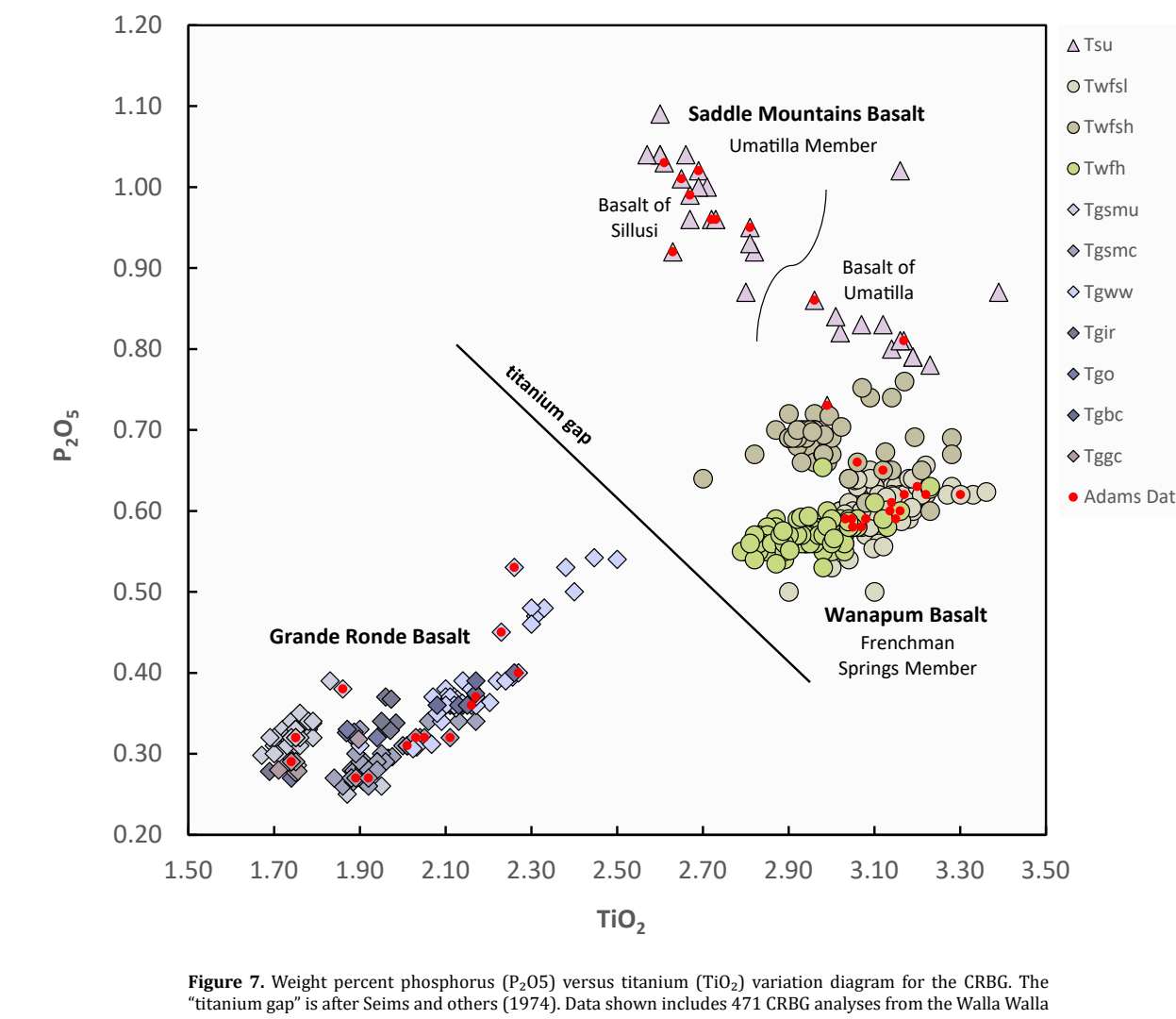

Figure 7. Weight percent phosphorus (P_2O_5) versus titanium (TiO_2) variation diagram for the CRBG. The "titanium gap" is after Seims and others (1974). Data shown includes 471 CRBG analyses from the Walla Walla and Umatilla River basins reported in this publication, Bush and others (1973), Kuehn (1995), Hutter (1997), Madin and Geitgey (2007), McClaughry and Azzopardi (2023), Madin and others (2023), and Guerrero and others (in press). Symbol colors are keyed to colors used for the geologic map units on Plate 1. The red-filled circles are 43 XRF analyses from this publication.

Table 1. Select geochemical analyses for Columbia River Basalt Group lava flows in the Adams 7.5′ quadrangle. Oxide content provided in weight percent (wt%) and trace element content in parts per million (ppm).

Sample	85 ATJ 2021	4 ADJ 2023	16 ATJ 2023	100 ATJ 2021	UMAT 5331 75[1]	UMAT 5331 125[1]	UMAT 5331 170[1]	UMAT 5331 360[1]	UMAT 5331 475[1]	UMAT 5331 550[1]	UMAT 5331 665[1]	UMAT 5331 800[1]	UMAT 5331 825[1]	UMAT 5331 895[1]	UMAT 5331 950[1]	UMAT 5331 1025[1]	UMAT 5331 1105[1]	UMAT 5331 1150[1]	UMAT 5331 1175[1]	UMAT 5331 1350[1]	UMAT 5331 1725[1]
Geographic Area	Gerking Creek Quarry	Athena-Waterman	Rainville Road	Adams	Adams (City Well)	Adams (City Well)	Adams (City Well)	Adams (City Well)	Adams (City Well)	Adams (City Well)	Adams (City Well)	Adams (City Well)	Adams (City Well)	Adams (City Well)	Adams (City Well)	Adams (City Well)	Adams (City Well)	Adams (City Well)	Adams (City Well)	Adams (City Well)	Adams (City Well)
Formation	Saddle Mountains	Saddle Mountains	Wanapum	Wanapum	Saddle Mountains	Wanapum	Wanapum	Wanapum	Saddle Mountains	Wanapum	Wanapum	Wanapum	Grande Ronde	Grande Ronde	Grande Ronde	Grande Ronde	Grande Ronde	Grande Ronde	Grande Ronde	Grande Ronde	Grande Ronde
Unit	Tsu (Basalt of Sillusi)	Tsu (Basalt of Umatilla)	Twfsl	Twfsl	Tsu (Basalt of Umatilla)	Twfsl	Twfsl	Twfsl	Twfsh	Twfsh	Twfh	Twfh	Tgsmu	Tgsmu	Tgsmc	Tgsmc	Tgsmc	Tgsmc	Tgww	Tgww	Tggc
Northing83HARN FT	1486407	1505077	1473677	1467867	1470105	1470105	1470105	1470105	1470105	1470105	1470105	1470105	1470105	1470105	1470105	1470105	1470105	1470105	1470105	1470105	1470105
Easting83HARN FT	1809115	1816394	1818244	1806070	1804905	1804905	1804905	1804905	1804905	1804905	1804905	1804905	1804905	1804905	1804905	1804905	1804905	1804905	1804905	1804905	1804905
Map Label	G36	G43	G33	G04	G07	G08	G09	G11	G12	G13	G14	G16	G17	G19	G20	G22	G24	G26	G27	G30	G31
Oxides, weight percent																					
SiO_2	54.43	53.28	51.70	52.00	55.65	51.93	51.35	51.41	52.12	51.74	51.54	52.16	54.55	55.12	53.1	54.03	54.78	54.23	55.05	56.08	55.66
Al_2O_3	13.53	13.39	13.01	13.31	13.31	13.17	13.28	13.43	13.19	13.31	13.53	13.75	14.31	14.09	14.29	14.41	13.93	13.93	13.35	13.23	13.86
TiO_2	2.73	3.17	3.05	3.08	2.61	3.14	3.17	3.2	3.06	3.12	3.05	2.65	1.75	1.75	1.89	2.11	2.05	2.16	2.23	2.26	1.74
FeOTotal	12.99	13.60	14.74	13.99	12.51	14.5	14.92	14.65	14.54	14.56	14.41	13.92	11.4	11.41	12.17	11.72	11.83	12.67	12.61	12.96	11.56
MnO	0.21	0.21	0.23	0.24	0.22	0.27	0.24	0.25	0.24	0.24	0.23	0.24	0.21	0.19	0.23	0.33	0.22	0.2	0.22	0.23	0.2
CaO	6.30	6.72	8.16	8.31	5.93	8.22	8.37	8.39	8.08	8.22	8.52	8.43	8.14	8.01	9.29	8.92	7.88	7.75	7.63	6.7	7.86
MgO	2.81	3.33	4.26	4.16	2.6	4.03	4.08	3.99	3.87	4.02	4.25	4.33	4.85	4.64	5.26	4.49	4.52	4.25	3.79	3.06	4.27
K_2O	2.59	2.26	1.55	1.47	2.79	1.45	1.23	1.31	1.44	1.34	1.15	1.16	1.38	1.39	0.75	0.81	1.36	1.34	1.65	1.78	1.55
Na_2O	3.44	3.23	2.70	2.86	3.36	2.69	2.74	2.75	2.81	2.81	2.74	2.83	3.1	3.08	2.75	2.86	3.1	3.11	3.01	3.17	3
P_2O_5	0.96	0.81	0.59	0.59	1.03	0.61	0.62	0.63	0.66	0.65	0.58	0.53	0.32	0.32	0.27	0.32	0.32	0.36	0.45	0.53	0.29
LossOnIgnition	0.49	0.86	0.35	0.57	3.06	3.19	4.49	4.59	3.55	4.37	5.33	3.77	3.16	2.9	3.68	2.3	1.2	3.67	0.81	3.48	2.41
TotalInitial	98.79	98.50	99.37	99.03	96.94	96.81	95.51	95.41	96.45	95.63	94.67	96.23	96.84	97.1	96.32	97.7	98.8	96.33	99.19	96.52	97.59
Trace Elements, parts per million																					
Ni	7	4	19	17	5	15	14	13	12	14	16	13	13	14	13	8	9	7	3	3	9
Cr	0	0	21	19	2	22	26	24	20	28	38	31	43	48	36	35	36	25	25	11	25
Sc	28	28	37	38	22	34	34	35	33	34	36	33	34	31	35	42	39	36	40	30	31
V	179	260	437	451	142	370	391	397	357	376	362	327	259	301	326	355	345	345	322	247	280
Ba	3427	2695	624	611	3400	601	573	564	556	588	494	711	556	578	375	467	498	475	588	774	570
Rb	39	37	37	34	48	36	35	38	41	37	32	28	36	39	21	19	38	37	38	49	40
Sr	276	271	309	311	nd	nd	nd	nd	nd	nd	nd	nd	nd	nd	nd	nd	nd	nd	nd	nd	nd
Zr	509	422	204	207	498	207	207	201	208	202	189	213	167	176	154	155	153	172	178	210	172
Y	50	46	45	45	49	45	45	44	44	43	40	40	34	36	33	34	34	34	40	44	32
Nb	23.2	21.7	15.7	14.8	23	16	16	16	16	16	15	15	11	13	12	12.6	12.3	13	13.6	16	12
Ga	24	22	22	22	nd	nd	nd	nd	nd	nd	nd	nd	nd	nd	nd	nd	nd	nd	nd	nd	nd
Cu	10	14	25	26	19	31	29	28	35	25	35	29	35	25	37	24	27	23	17	11	29
Zn	130	127	145	148	120	136	136	147	143	142	138	123	101	109	112	127	118	127	131	135	120
Pb	12	10	7	7	9	8	9	8	9	9	8	9	9	8	6	4	6	8	6	10	9
La	46	39	28	27	49	29	28	30	27	30	28	27	23	24	21	12	13	23	30	29	21
Ce	96	85	52	56	88	56	55	53	49	54	50	52	43	44	41	30	37	42	55	59	42
Th	6	6	3	3	9	5	4	5	5	5	7	3	4	6	4	3	5	4	3	7	6
Nd	50	45	34	36	nd	nd	nd	nd	nd	nd	nd	nd	nd	nd	nd	nd	nd	nd	nd	nd	nd
U	3	1	2	1	2	0.8	1.6	0.8	nd	1.3	1.1	nd	nd	nd	1	nd	nd	0.8	nd	2.1	1.4

Major element determinations have been normalized to a 100-percent total on a volatile-free basis and recalculated with total iron expressed as FeOTotal; nd - no data or element not analyzed; na - not applicable or no information.
TotalInitial, original analytical total. Samples from [1]USGS/OWRD, https://apps.wrd.state.or.us/apps/gw/gw_info/gw_info_report/gw_details.aspx?gw_site_id=1008

Table 2. Electron microprobe glass-shard analyses from tephra in the Adams 7.5′ quadrangle. Average (Avg.) and standard deviation (Std. Deviation) of sample oxide content provided in weight percent (wt%).

Sample	SHP1 160		DGSH North1		24a JDM 2024		26 JDM 2024		2 ADJ 2023	
Geographic Area	Sand Hollow		Sand Hollow		Gerking Flat		Gerking Flat		Sand Hollow	
Formation	na		na		na		na		na	
Unit	Qlo		Qlo		Qlo		Qlo		Qlo	
Northing83HARN FT	1496085		1503960		1495542		1495252		1504316	
Easting83HARN FT	1798067		1793214		1806545		1806764		1792616	
Map Label	G39		G43		G38		G37		G45	
Oxides, weight percent	**Avg.**	**Std. Deviation**	**Avg.**	**Std. Deviation**	**Avg.**	**Std. Deviation**	**Avg.**	**Std. Deviation**	**Avg.**	**Std. Deviation**
SiO_2	73.06	0.38	72.62	0.44	72.69	0.63	72.65	0.38	73.56	0.44
Al_2O_3	14.06	0.33	14.44	0.28	14.34	0.25	14.38	0.25	13.94	0.29
TiO_2	0.41	0.02	0.42	0.03	0.41	0.04	0.41	0.02	0.16	0.02
Fe_2O_3	2.06	0.06	2.12	0.08	2.11	0.2	2.09	0.07	2.24	0.07
CaO	1.55	0.10	1.56	0.08	1.63	0.17	1.61	0.11	0.97	0.08
MgO	0.45	0.02	0.46	0.03	0.47	0.06	0.46	0.02	0.17	0.02
K_2O	2.67	0.13	2.75	0.13	2.76	0.14	2.67	0.1	3.04	0.14
Na_2O	5.55	0.27	5.43	0.22	5.41	0.16	5.54	0.14	5.79	0.3
Cl	0.18	0.10	0.19	0.05	0.18	0.02	0.17	0.01	0.15	0.01
Number of shards	20		28		29		26		17	
Similarity Coefficient	1		0.98		0.98		0.98		~0.97	
Probable correlation and age	Mazama 7,700 cal yr. B.P.		Mazama 7,700 cal yr. B.P.		Mazama 7,700 cal yr. B.P.		Mazama 7,700 cal yr. B.P.		Walker Lake 5-42A ~171-130 ka	

SI (International System) Metric to U.S. Customary Units

	Original Units	Conversion Equation	To obtain
length:	millimeter (mm)	mm x 0.039	inch (in)
	centimeter (cm)	cm x 0.394	inch (in)
	meter (m)	m x 3.281	foot (ft)
	meter (m)	m x 1.094	yard (yd)
	kilometer (km)	km x 0.621	mile (mi)
area:	square kilometer (km^2)	km^2 x 0.386	square mile (mi^2)
volume:	cubic kilometer (km^3)	km^3 x 0.240	cubic mile (mi^3)

REGISTERED GEOLOGIST
OREGON
CARLIE AZZOPARDI
Expires: 06/30/2026